ROLLING ELEMENT SKEW MEASUREMENT IN A SPHERICAL ROLLER BEARING UTILIZING A CPD PROBE

A Thesis
Presented to
The Academic Faculty

By

Daniel Osorno

In Partial Fulfillment
of the Requirements for the Degree
Master's of Science in Mechanical Engineering

Georgia Institute of Technology
December 2005

**ROLLING ELEMENT SKEW MEASUREMENT IN A SPHERICAL ROLLER
BEARING UTILIZING A CPD PROBE**

Approved by:

Steven Danyluk, Ph.D., Chair
School of Mechanical Engineering

Shreyes Melkote, Ph.D.
School of Mechanical Engineering

David Sanborn, Ph.D.
School of Mechanical Engineering

Date Approved: August 23, 2005

This thesis is dedicated

to my parents

who have been behind

every accomplishment

in my life.

ACKNOWLEDGEMENTS

First I would like to give special thanks to my advisor, Dr. Steven Danyluk for all the support, guidance, and advice provided to me during my undergraduate and graduate career.

I want to thank Dr. Melkote and Dr. Sanborn for their time and effort in serving on my thesis committee. Both were teachers of mine during my studies at the Georgia Institute of Technology and the knowledge parted to me has proven invaluable. I would like to thank Dr. Zharin for the input and efforts in designing new probes circuitries for my utilization, The George W. Woodruff School of Mechanical Engineering for the use of their facilities and staff, including but not limited to the student machine shop, the Precision Machining Center, and the office of graduate studies. I would also like to thank my lab mates for their support and advice, specially Siarhei Tsiareshka for helping me develop probes, Frank Mess for giving me advice, my brother Andres Osorno for encouraging me through my studies, and Yuri Pyekh for troubleshooting some LabVIEW issues.

I would also like to thank Mike Kotzalas and Mike Hoeprich from Timken for helping me during the conceptual part of the experiments, providing me with Timken equipment for testing during the experiments, and for all their invaluable advice.

Finally, I would also like to thank you, Mom and Dad, for always being there. Your support is what helped me make it through this endeavor. And most importantly, thank you God for blessing me with such wonderful people in my life, and for being my guide.

TABLE OF CONTENTS

LIST OF TABLES

LIST OF FIGURES

SUMMARY

This thesis incorporates an array of Contact Potential Difference (CPD) sensors to measure and monitor the degree of skew in the rolling elements of a spherical roller bearing. Skewing is the motion of a roller as it turns about an axis normal to the roller race interface. Roller skew is generated as part of the kinematic effects of roller bearings. Skew monitoring is important for bearing design as it is an indirect measure of bearing life.

For the purpose of this thesis, roller skew was measured utilizing multiple pairs of CPD probes located around the bearing's outer raceway at varying points of the loading zone. These CPD probes are not in direct contact with the rollers, but in close proximity to their surface (through the bearing outer ring). The skew angle measured is related to different operating conditions such as applied load, shaft speed, and lubrication.

The pair of CPD probes detected a signal as the roller surface passed by and the phase difference between the two distinct signals measured the skew angles in the range of 0.016° to 1.10°. The shaft is rotated both clockwise and counterclockwise to capture any probe misalignment which was in the range of 0.5° up to 2.0° . This thesis also provides a model for the probe signal as a spherical roller surface passes the probe surface.

CHAPTER 1

INTRODUCTION

This thesis addresses the use of a non-vibrating Kelvin probe to monitor a spherical roller bearing while in operation under different loading conditions. The non-vibrating Kelvin probe functioning as a capacitance sensor with the difference being that there are no externally applied voltages to the sensor. For the measurement of skew angle, a pair of probes was necessary in order to have two signals: a reference and a measurement signal. These probes were placed at different points of the loading zone, allowing for a simultaneous monitoring of the roller skew at these points.

Kelvin probe sensors measure contact potential difference (CPD) which is related to the change in surface potential or work function of the surface of interest. The work function is the minimum energy required to remove an electron from the Fermi energy level to just outside the conductor surface. To perform CPD measurements, Kelvin probes generally use relative motion, either vibration or translation of one surface relative to the other (i.e. probe surface relative to surface of interest).

The objective of this thesis was to use the non- vibrating CPD sensor to monitor skew along an operating spherical roller bearing, and use the resulting phase difference between the pair of signals to determine the roller skew angle. Furthermore, since skew is related to torque, and torque is inversely related to the working lifetime of the bearing, this thesis suggests a scheme to monitor spherical roller bearings to improve their design so as to minimize skew and increase working lifetime.

CHAPTER 2

BACKGROUND

Surface Potential of Conducting Materials

The work function, Φ, of a conductor is defined as the energy required to remove an electron from the Fermi energy level to just outside the surface or the vacuum reference level. Figure 1 illustrates the electronic band structure and the potential well of a conductor in a vacuum at absolute zero. The potential energy just outside the surface is defined as zero and the work function, Φ, is the lowest energy required to remove an electron from the bulk material to just outside the surface. It is the difference in work function between two materials that defines contact potential difference.

Potential
Energy per
electron

Conductor Surface

Work function, Φ
Minimum energy
required to move an
electron from the Fermi
energy level to outside
of the conducting
material

E_f: Fermi Level

Pairs of electrons per
energy state: one with
spin up and the other
with spin down
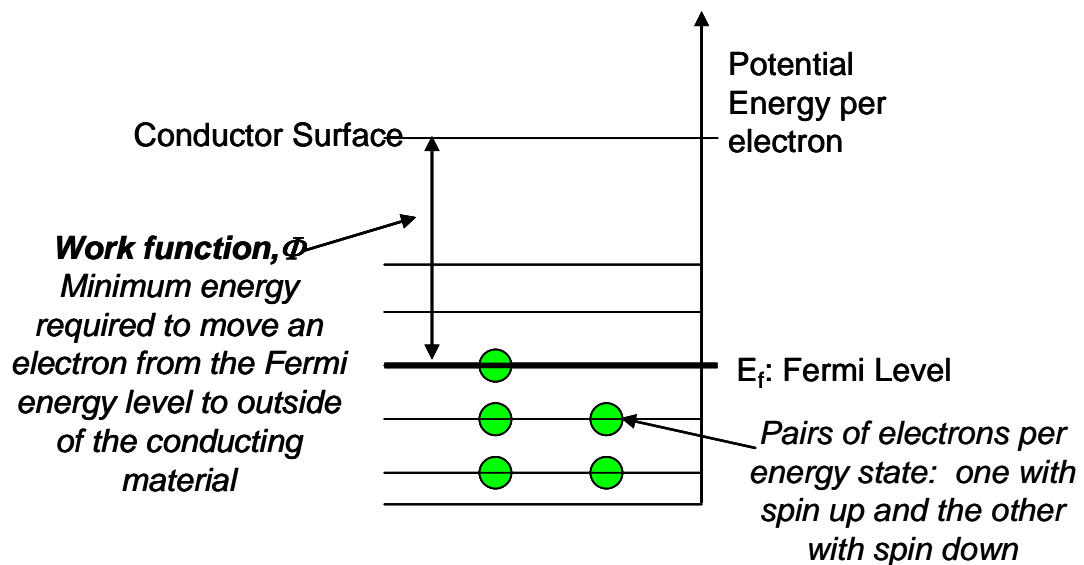
Figure 1. Electronic band diagram of a conductor in a vacuum at absolute zero [1].

Definition of Contact Potential Difference

Contact potential difference (CPD) can be used to monitor the chemical and mechanical changes of electrically connected surfaces and one such scheme, shown in Figure 2, shows a schematic diagram of the band structure of two conducting materials not in contact.
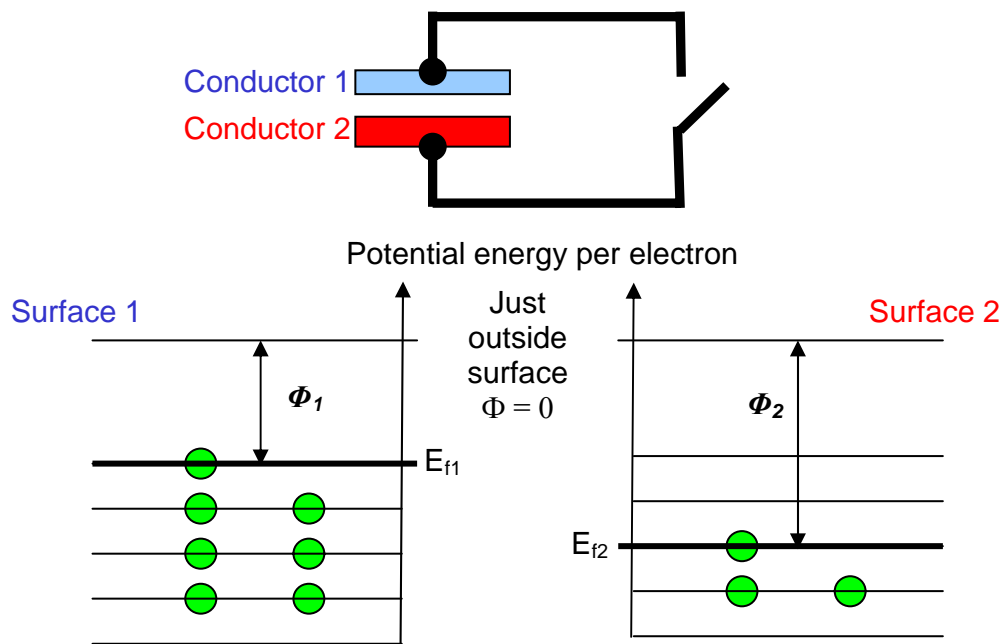
Figure 2. Energy level diagram of the work function of two metals in close proximity with no electrical contact [1].

Each conductor has it's Fermi energy, and the potential energy of both surfaces is taken as zero just outside the surface. When these two conductors are electrically connected, as shown in Figure 3, electrons will flow from the material with the higher potential energy (labeled as Conductor 1) to the one with the lower potential energy (Conductor 2). The charge flow will appear instantaneous and cease when the Fermi

energies equilibrate. This transfer of electrical charge will result in a net negative charge in one material balanced by a positive charge in the other. With the Fermi energy being chosen as the new reference of potential, the voltage between these two can be related to the work function of each material (Φ_1 and Φ_2) by:

$$\Delta V = \frac{\Phi_2 - \Phi_1}{|e|}$$

Equation 1

where e is the charge of an electron and ΔV, or V_{CPD}, is defined as the contact potential difference of the two conductors.
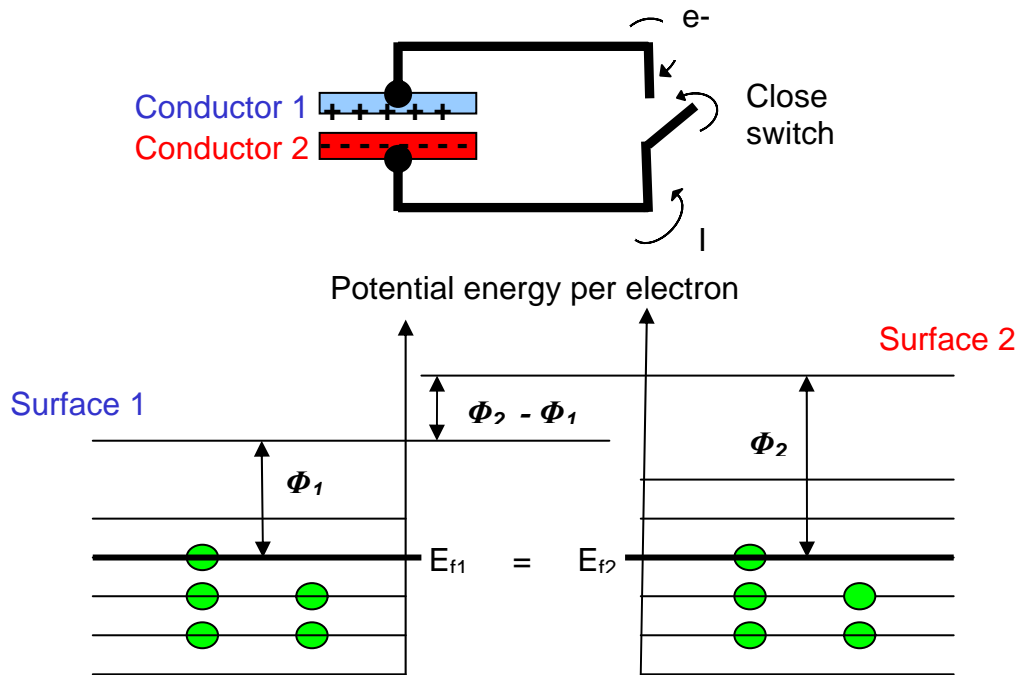
Figure 3. Energy level diagram of the work function of two metals in close proximity with electrical contact [1].

The charge on the surfaces and contact potential are related by:

$$q = C(\Phi_2 - \Phi_1) = CV_{CPD}$$

Equation 2

where C is the constant of proportionality, the capacitance that develops between the surfaces. In order to simplify the model, it is assumed that the surfaces are flat and therefore comprise a parallel plate capacitor. Thus the charge on the surfaces, q, is related to capacitance, C, and contact potential difference (Vcpd) as:

$$q = CV_{CPD}$$
Equation 3

where the capacitance for a parallel plate geometry is given by:

$$C = \frac{\varepsilon_r \varepsilon_o A}{d}$$
Equation 4

where ε_r is the relative dielectric constant, ε_o is the permittivity of free space, A is the area of surfaces, and d is the spacing between the two plates.

If either a relative motion between the two surfaces exists, or a change in surface characteristics occurs with time, the resultant current that would flow between these two surfaces is described by:

$$i = \frac{dQ}{dt} = \frac{d(CV_{CPD})}{dt} = V_{CPD}\frac{dC}{dt} + C\frac{dV_{CPD}}{dt}$$
Equation 5

where the first term $V_{CPD}\frac{dC}{dt}$ is considered as the geometry term and the second term

$C\frac{dV_{CPD}}{dt}$ is considered as the chemistry term.

Kelvin Probe

The Kelvin probe is a capacitor sensor that measures the contact potential difference (CPD) between two dissimilar conducting materials with no externally applied

voltages or currents.. In 1898, Lord Kelvin proposed that this potential difference could be measured by a gold leaf electroscope [2]. This response was momentary and difficult to quantify. In 1932 the probe was modified by Zisman such that one electrode vibrated with respect to the other [3]. He proposed that the change in spacing between the two electrodes or time varying capacitance created a current proportional to the CPD between the two metals. Thus if the work function of the vibrating electrode was known, the work function of the other metal could be determined. This probe is typically used to study the work function and surface potentials of metals and dielectrics.

Non-Vibrating Contact Potential Difference Sensor

An alternate method to obtain CPD measurements proposed by Danyluk and Zharin is using translation [4]. Relative motion of the surface will result in electrical signals if there are geometrical or chemical changes on the surface. The signal will reflect time varying changes in the contact potential difference of the surfaces, rather than the absolute CPD as in the case of the Kelvin probe.

Rolling Element Skew Measurement

The concept of utilizing a CPD measurement technique in order to calculate the skew of rolling elements in a bearing was first employed by Yang and Danyluk in 2000 [5]. Their work consisted of utilizing CPD probes to measure roller skew in tapered roller bearings at different running conditions. The measurement of the roller skew is important as it relates to the lifetime of the bearing. In a well designed bearing, the

roller-cage loads due to roller skewing motions may be minimized, thereby increasing the lifetime of the bearing. Due to slightly imperfect bearing geometries there exists an inevitable tendency for unbalance of frictional loading between the roller-inner raceway and roller-outer raceway contacts. This loading unbalance generates roller skew which is detrimental to the roller bearing operation because it causes increased friction torque and frictional heat generation as well as the requirement for a cage strong enough to resist the roller moment loading.

Roller skew will be measured utilizing a pair of CPD probes aligned next to each other with a known horizontal distance. When a roller skews, as displayed in Figure 4, its surface passes one of the CPD probes prior to the other. Each separate CPD probe records a waveform for the portion of the surface it is able to measure, and the phase difference between both waveforms is construed as the roller skew.
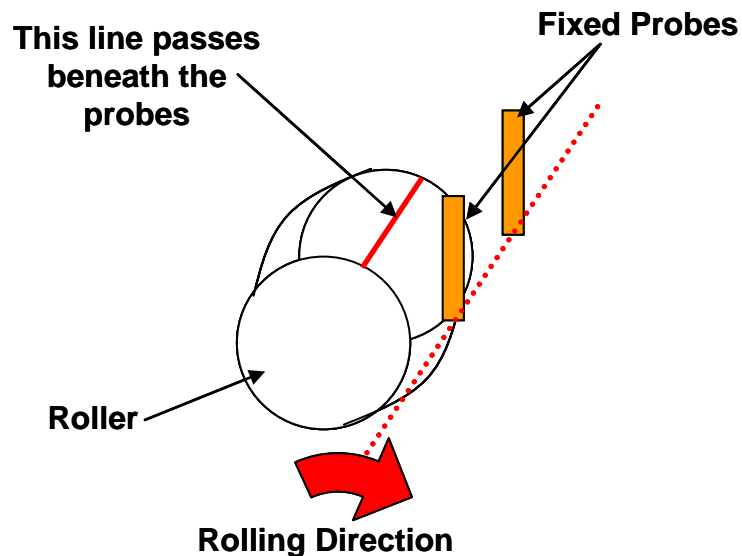
Figure 4. Roller skew measurement technique (top view)

Roller CPD waveform

The CPD signal expected from the rotation of a roller can be estimated by combining rolling kinematics to a capacitance model. For this, geometrical relationships were obtained and evaluated as seen in Figure 5 below [6].
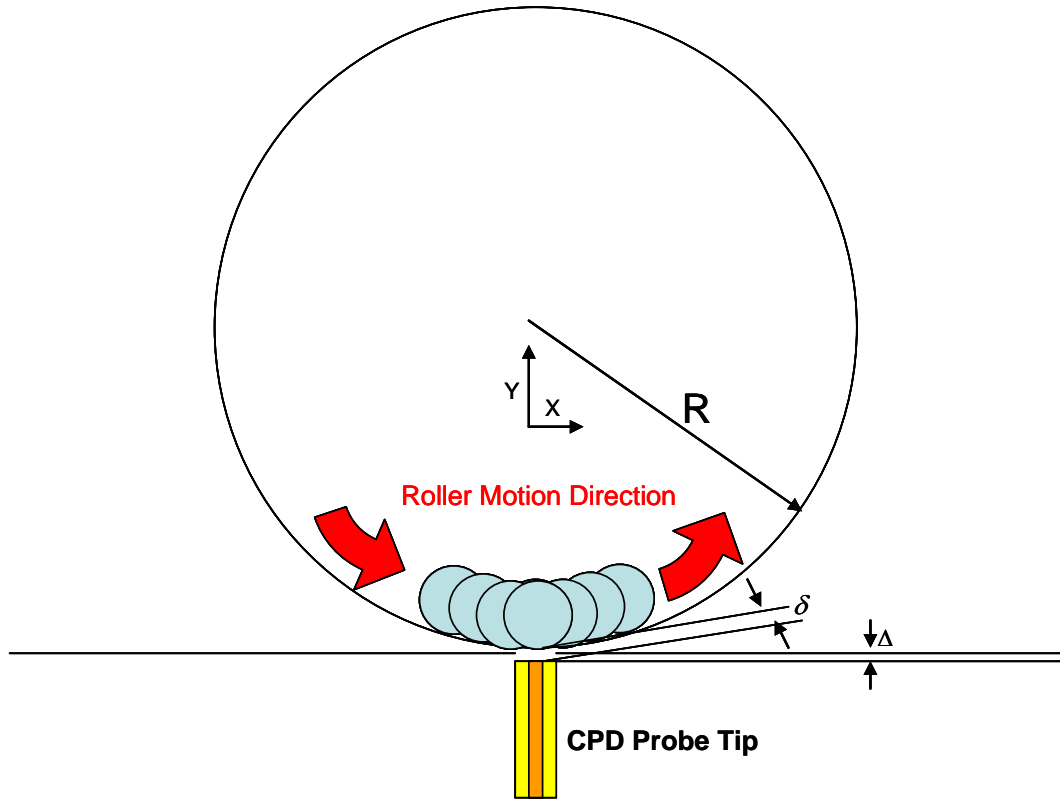
Figure 5. Roller kinematics and capacitance

Based on the variables in Figure 5, a relationship to calculate δ is found

$$\delta = \left[(R + \Delta)^2 + x^2 \right]^{\frac{1}{2}} - R - \Delta \qquad \text{Equation 6}$$

and taking the derivative of δ yields

$$\frac{\partial \delta}{\partial t} = \frac{1}{2} \left[(R + \Delta)^2 + x^2 \right]^{-\frac{1}{2}} 2x \frac{\partial x}{\partial t} \qquad \text{Equation 7}$$

For a plate capacitor

$$C = \frac{k}{\delta}$$
<div align="right">Equation 8</div>

and

$$C = \frac{q}{v}$$
<div align="right">Equation 9</div>

Where q is charge and v is voltage, thus

$$q = v\frac{k}{\delta}$$
<div align="right">Equation 10</div>

Assuming that V is constant and that there is no impedance of consequence present in the measurement Equation 11 is obtained

$$current = \frac{\partial q}{\partial t} = -\frac{k}{\delta^2}\frac{\partial \delta}{\partial t}$$
<div align="right">Equation 11</div>

Equation 11 is then combined with Equation 7 to obtain

$$\frac{\partial q}{\partial t} = -\frac{k}{\delta^2} \times \frac{1}{2}\left[(R+\Delta)^2 + x^2\right]^{-\frac{1}{2}} 2x\frac{\partial x}{\partial t}$$
<div align="right">Equation 12</div>

Equation 12 is then solved in to obtain

$$\frac{\partial q}{\partial t} / k = -\frac{-x}{\left[\left[(R+\Delta)^2 + x^2\right]^{-\frac{1}{2}} - R\right]^2 \times \left[(R+\Delta)^2 + x^2\right]^{\frac{1}{2}}}$$
<div align="right">Equation 13</div>

Using Equation 13 a chart for the expected CPD signal from the rollers can be obtained. Based on the geometry of the system used, Figure 6 is obtained by plotting the distance along the raceway on the x-axis and the change in charge on the y-axis. This graph models the expected CPD signal output for each roller.
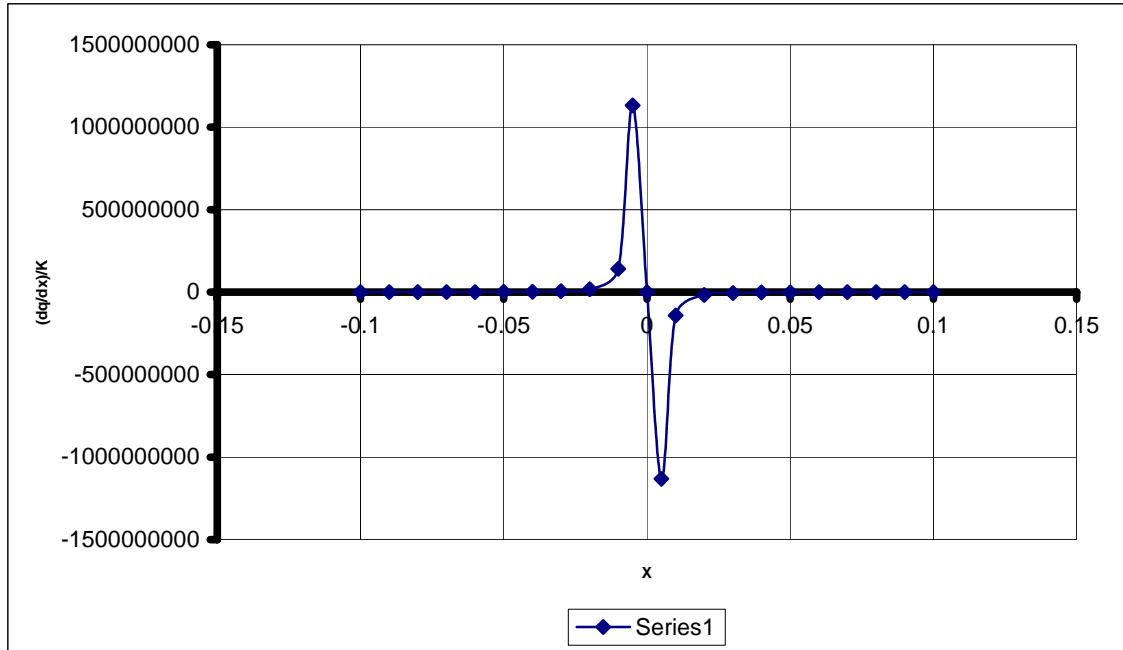
Figure 6. Theoretical roller CPD signal

Spherical Roller Bearings

Spherical roller bearings have an outer raceway that is a portion of a sphere shell; hence, the bearings are internally self-aligning. Each roller has the form of a barrel, with a curved generatrix (A geometric element that generates a geometric figure, especially a straight line that generates a surface by moving in a specified fashion) in the direction transverse to rotation that conforms relatively closely to the inner and outer raceways. This shape characteristic provides for the spherical roller bearing's high load-carrying capacity. For the purpose of this thesis, Torrington 22208CJW33C4 spherical roller bearings were used. A representative drawing of the shape of such bearings is displayed in Figure 7 and its dimensions are shown in Figure 8.
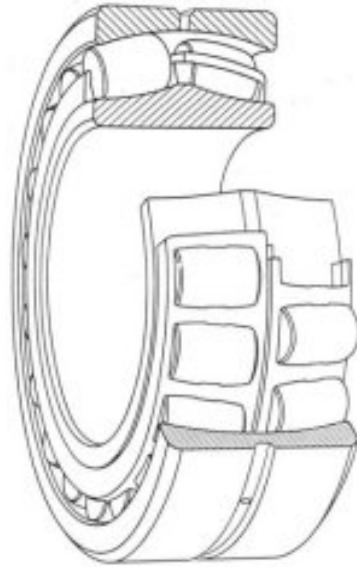
Figure 7. Spherical roller bearing

C= 23mm
d= 40mm
D= 80mm
E= 50mm
F= 72mm
r= 1mm
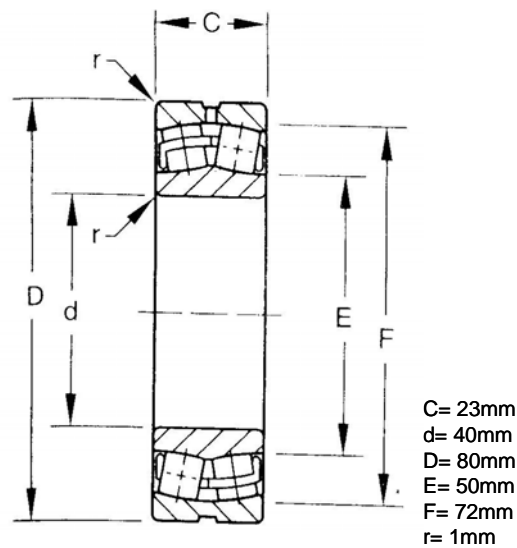
Figure 8. 22208CJW33C4 dimensions

As it can be observed in Figure 4, the spherical roller bearings have double-row symmetrical barrel rollers. Because of the close contact between the rollers and raceways and the curved generatrices, spherical roller bearings have inherently greater friction than cylindrical roller bearings. This is due to the degree of sliding that occurs in the roller-

raceway contracts. Spherical roller bearings are therefore not readily suited for use in high speed operations, but perform well in heavy load applications [7].

Roller Skewing in Spherical Roller Bearings

In spherical roller bearings with symmetrical roller profiles, proper management of roller skewing can reduce frictional losses and corresponding friction torque generated. The temperature rise associated with friction is the factor that limits performance in many applications. Designing the bearings so that skewing equilibrium is provided by the raceway guidance alone lowers losses and increases load-carrying capacity.

Any rolling element that contacts a raceway along a curved contact surface will undergo sliding in the contact. For an unskewed roller there will be at most two points along each contact where the sliding velocity is zero. The zero sliding points form the generatrices of a theoretical rolling cone, which represents the contact surface on which pure kinematic rolling would occur for a given roller orientation. At all other points along the contact, sliding is present in the direction of rolling or opposite to it, depending on whether the roller radius is greater or less than the radius to the theoretical rolling cone, as illustrated in Figure 9 [7].
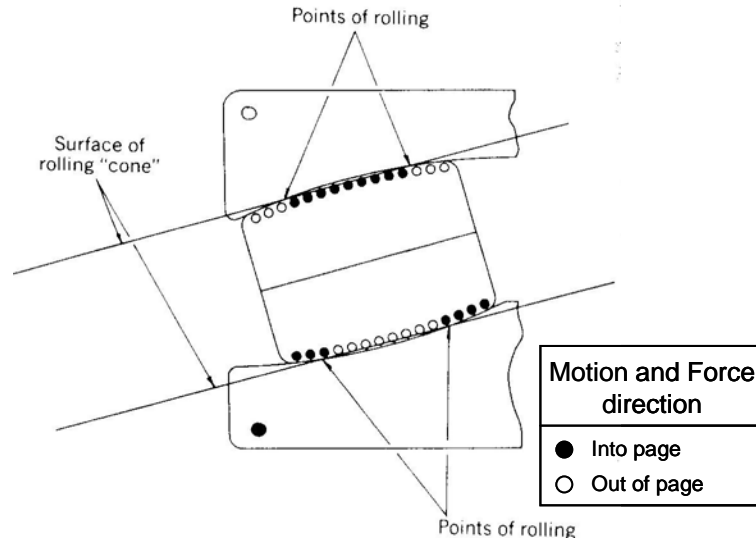
Figure 9. Spherical roller bearing, symmetrical roller-tangential friction forces

Friction forces or tractions due to sliding will be oriented to oppose the direction of sliding on the roller. In the absence of tangential roller forces from cage or flange contacts, the roller-raceway traction forces in each contact must sum to zero. Additionally, the sum of the inner and outer raceway contact skewing moments must equal zero. These two conditions will determine the position of the rolling points along the contacts and thus the theoretical rolling cone. These conditions are met at the equilibrium skewing angle. If the moments tend to restore the roller to the equilibrium skewing angle when it is disturbed, the equilibrium skewing angle is said to be stable [7].

As a roller skews relative to its contacting raceway a sliding component is generated in the roller axial direction and traction forces are developed that oppose axial sliding. These traction forces may be beneficial in that, if suitably oriented, they help to carry the axial bearing load.

The motion and force direction distribution in Figure 9 is what determines the extent of skew that will be present for a particular roller. The skewing moment produced

by the imbalance of forces is augmented by unbalance or raceway-roller friction forces as shown in Figure 10.

$$Q_{oj}$$

q_{ojk} τ_{ojk}

Q_{aj}

Q_{aj}

τ_{ijk}

q_{ijk}

Legend	
Q	Roller Load
q	Load per unit length
T	Shear Stress

$$Q_{ij}$$
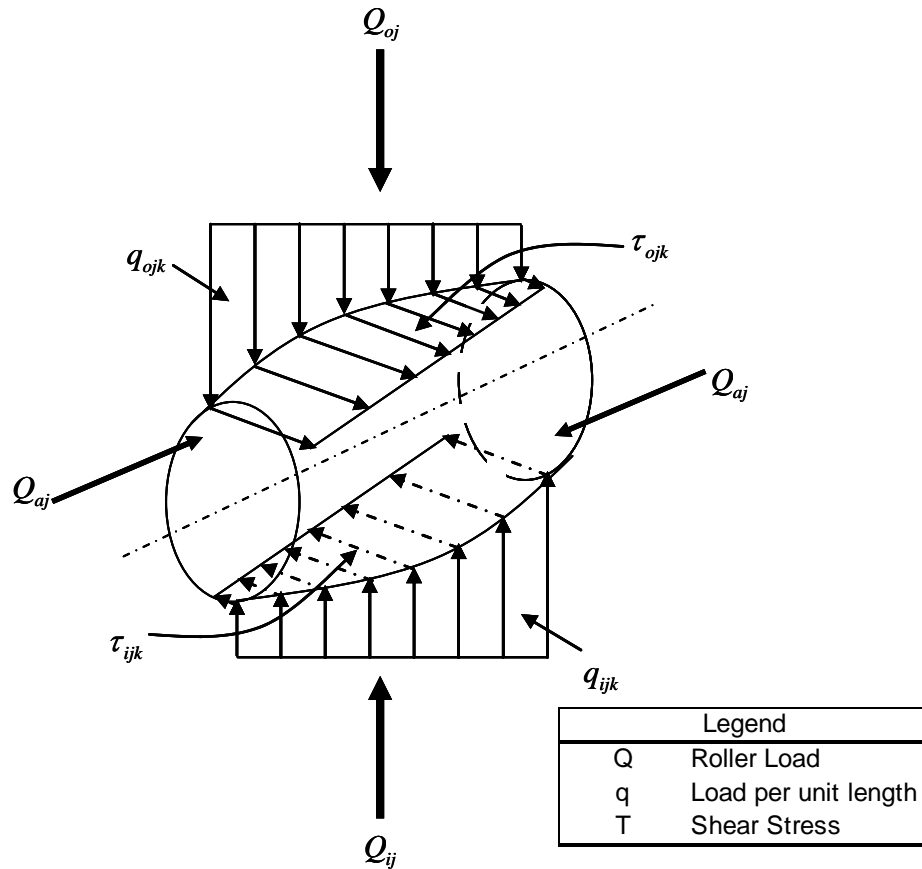
Figure 10. Normal, axial, and frictional loading of a roller at azimuth

Motivation

The measurement of skew is an important factor that needs to be taken into consideration for bearing design due to its relationship to fatigue life in a bearing. Such a relationship is extremely complicated and highly dependent upon the geometric characteristics of the bearing, lubricating conditions, material selection, environmental conditions, and loading conditions. Therefore, over the course of this section, an

explanation to the mechanisms which relate skew to fatigue life will be given without specifically assigning experimental conditions. The flowchart displayed in Figure 11 summarizes the methodology path taken to link skew to fatigue life. When loaded radially, rollers in the bearing are squeezed at one end and thereby forced against the outer and inner raceways. This causes a roller-raceway frictional force and hence a roller skewing moment that must be substantially resisted by the cage.

```
                    ┌──────────┐
                    │   Skew   │
                    └────┬─────┘
                         ↓
                    ┌──────────┐
                    │ Sliding  │
                    └────┬─────┘
                         ↓
               ┌───────────────────┐
               │ Heat Generation   │
               └────────┬──────────┘
                        ↓
             ┌──────────────────────┐
             │ Temperature Increase │
             └──────────┬───────────┘
                        ↓
           ┌──────────────────────────┐
           │ Reduced Lubricant Viscosity │
           └────────────┬─────────────┘
                        ↓
        ┌────────────────────────────────┐
        │ Reduced Lubricant Film Thickness │
        └───────────────┬────────────────┘
                        ↓
              ┌─────────────────────┐
              │ Lubrication Factor  │
              └──────────┬──────────┘
                        ↓
  ┌──────────────────────────────────────────────────┐
  │ Reduced Film Thickness-to-Surface Roughness Ratio │
  └───────────────────────┬──────────────────────────┘
                        ↓
              ┌─────────────────────┐
              │ Reduced Fatigue Life │
              └─────────────────────┘
```
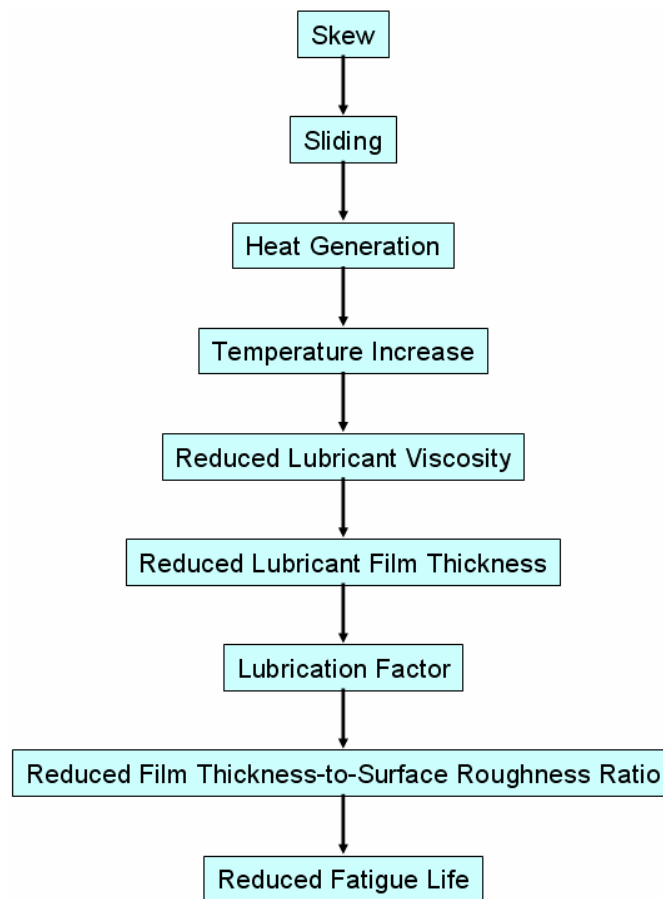
Figure 11. Flowchart linking skew to fatigue life

Although rolling bearings are designed to minimize friction in rotating shafts, they exhibit a small amount of friction during rotation. If friction is not present, the rolling elements would slip on the rotating surfaces rather than roll.

When in motion, a portion of the roller velocity is taken axially, which is pure sliding, and the remainder is taken in the rolling direction, which is pure rolling. Due to the kinematics of bearing operation, the torque in the bearing increases as the sliding velocity is increased. Since the roller is inclined towards attaining a minimum energy state, it will skew to accommodate itself to the working conditions. The roller velocity portion in the rolling direction would be lower if the roller did not skew, making the sliding velocity in the rolling direction larger.

As the sliding velocity increases, the heat generation in the system increases by:

$$H_f = \frac{1}{C} \int_{ContatArea} V_{sliding} \times \tau_{shear} \qquad \text{Equation 14}$$

where C is a constant converting Newton-meters per second to watts. As heat generation increases, so does the temperature of the system [8].

Lubricant viscosity is extremely sensitive to both pressure and temperature. Roelands [10] noted that at constant pressure the viscosity increases almost exponentially with the reciprocal of absolute temperature as shown by:

$$\log(\log \eta + 1.200) = -S_0 \log\left(1 + \frac{t_m}{135}\right) + \log G_0 \qquad \text{Equation 15}$$

where η is the absolute viscosity in centipoise, t_m is the temperature in °C, G_0 is a dimensionless constant indicative of viscosity grade of the liquid, and S_0 is a dimensionless constant that establishes slope of viscosity-temperature relationship.

Therefore, if the temperature increases, the viscosity of the lubricant decreases.

The formation of the lubricant film between the mating bearing surfaces is called the elastohydrodynamic (EHD) mechanism of lubrication. The two major considerations in EHD lubrication are the elastic deformation of the contacting bodies under load and the hydrodynamic effects forcing the lubricant to separate the contacting surfaces while the pressure of the load is deforming them [11].

The lubricant film thickness between two contact surfaces can be related to bearing performance. The thickness of the generated film depends on operating conditions such as velocity, load, lubricant viscosity and the relationship of pressure to viscosity [12].

Lubricant film thickness in the contact of the bearing roller-inner raceway is proportional to viscosity as shown by [13]:

$$H^* = \frac{1.6 G^{0.6} U^{0.7}}{W^{0.13}}$$
<div style="text-align:right">Equation 16</div>

where H is a dimensionless film thickness, G is a dimensionless materials parameter, U is a dimensionless speed parameter, and W is a dimensionless load parameter.

In Equation 16, the film thickness is related to viscosity through the dimensionless materials parameter G. This parameter is [14]:

$$G = \xi E'$$
<div style="text-align:right">Equation 17</div>

where ξ is the pressure-viscosity coefficient in meter square per Newton, and E' is effective elastic modulus. The pressure-viscosity coefficient is described by:

$$\xi = \left| \frac{\partial \ln(\mu)}{\partial p} \right|_{p=0}$$
<div style="text-align:right">Equation 18</div>

In Figure 12, it can be observed that as relative viscosity increases, so does the life adjustment factor. Likewise, in Figure 13 it can be observed that as the ratio of the film thickness-to-surface roughness decreases (i.e. bearings run hotter) the fatigue life decreases.
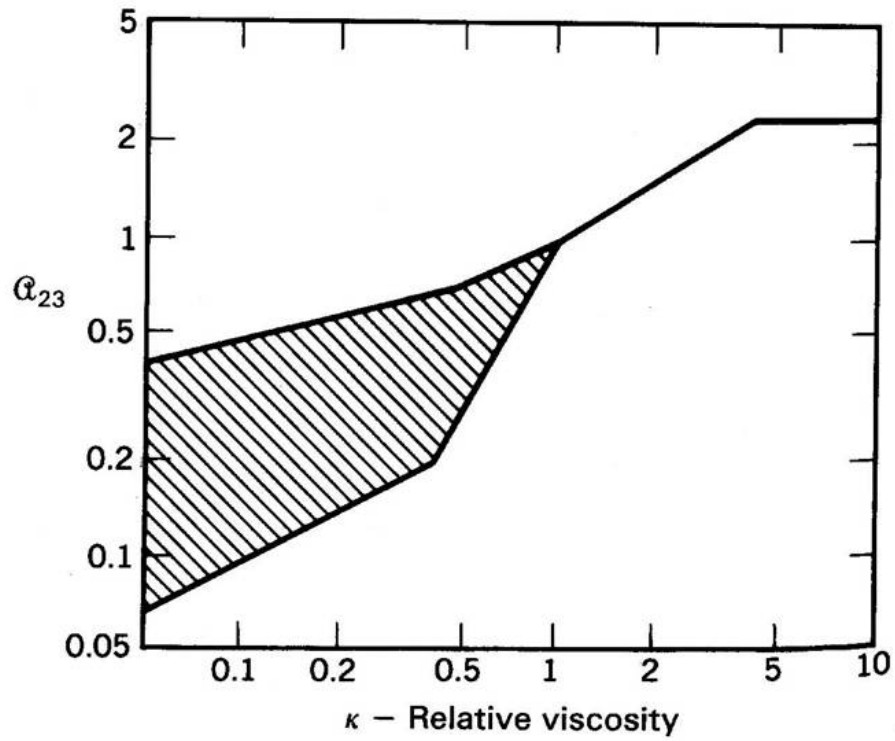

Figure 12. Material lubrication life factor plotted as a function of lubricant relative viscosity [8]
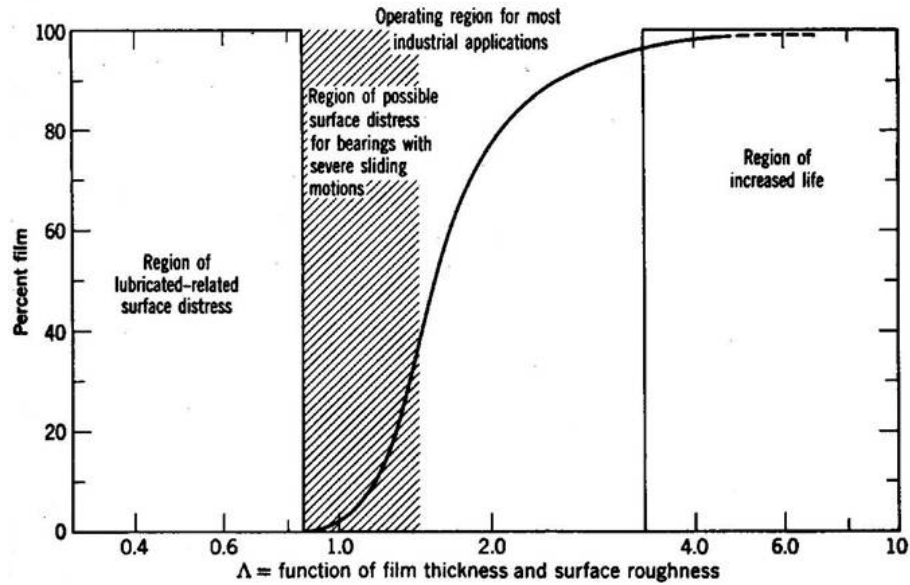
Figure 13. Percent film thickness vs Lambda function [8]

Load Carried by Roller

The loads carried by roller bearings are transmitted through the rolling elements from one raceway to the other. The magnitude of the load carried by the individual roller depends on the internal geometry of the bearing and on the type of load applied to it. In addition to applied loading, rolling elements are subjected to dynamic loading due to speed effects, and these dynamic loadings are in turn affected again by the geometry of the bearing.

A rolling element can support a normal load along the line of contact between the rolling element and the raceway. If a radial load Q_r is applied to the double-row symmetrical roller spherical roller bearing as displayed in Figure 14,

19
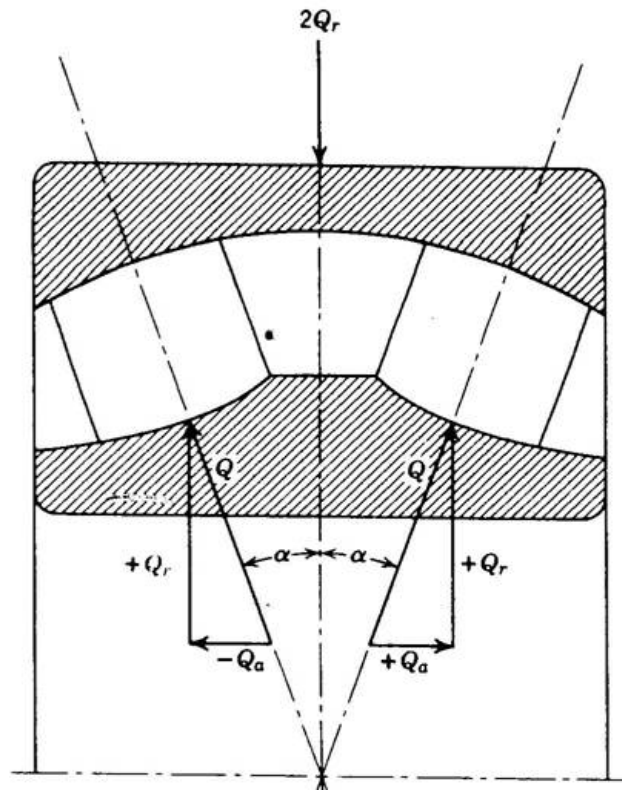
Figure 14. Radially loaded symmetrical spherical rollers [8].

then the normal load supported by the roller is

$$Q = \frac{Q_r}{\cos \alpha}$$

Equation 19

Hence a thrust load of magnitude

$$Q_a = Q \times \sin \alpha$$

Equation 20

or

$$Q_a = Q_r \times \tan \alpha$$

Equation 21

is induced in the assembly. For the double-row spherical roller bearing under an applied radial load the induced roller thrust loads are self-equilibrating as seen previously in Figure 14.

Load-Deflection Relationships

Understanding the load-deflection relationship equations displayed in this chapter are a necessary preliminary step to accurately calculate the extent of the loading zone in the spherical roller bearings being tested. Equation 22 below shows the relationship between the roller load Q and the deflection or contact deformation δ. For this equation, K is the axial load deflection factor in millimeters and the exponent n=1.11 for roller bearings (assuming that there exists a line contact between the surfaces).

$$Q = K\delta^n \qquad \text{Equation 22}$$

The total normal approach between two raceways under load separated by a rolling element is the sum of the approaches between the rolling element and each raceway as shown in Equation 23.

$$\delta_n = \delta_i + \delta_o \qquad \text{Equation 23}$$

Therefore

$$K_n = \left[\frac{1}{\left(1/K_i\right)^{\frac{1}{n}} + \left(1/K_o\right)^{\frac{1}{n}}} \right]^n \qquad \text{Equation 24}$$

and

$$Q = K_n \delta^n \qquad \text{Equation 25}$$

For steel roller and raceway contact with roller length l,

$$K_{linecontact} = 7.86 \times 10^4 l^{\frac{8}{9}} \qquad \text{Equation 26}$$

With these relationships, the extent of the loading zone in the spherical roller bearing subjected radial loads is calculated as shown in the forthcoming section.

Loading Zone Calculation

Calculation of the loading zone is necessary in order to accurately pinpoint the location for the placement of the CPD probes and to further understand the results obtained at each location. Having determined previously how each roller in a bearing carries load, it is possible to determine how the bearing load is distributed among the rollers.

Most rolling bearing applications involve steady state rotation of either the inner or outer raceway or both; however, the speeds of rotation are usually not so great as to cause roller centrifugal forces or gyroscopic moments of magnitude large enough to significantly affect the distribution of applied loads among the rolling elements. Furthermore, in most applications the frictional forces and moments acting on the rolling elements also should not significantly influence this load distribution. Consequently, in analyzing the distribution of rolling element loads, it is usually satisfactory to ignore these effects in most applications [9].

For a rigidly supported bearing subjected to radial load, the radial deflection at any rolling element angular position is given by Equation 27

$$\delta_\psi = \delta_r \cos\varphi - \frac{1}{2}P_d \qquad \text{Equation 27}$$

for which δ_r is the raceway radial shift occurring at $\varphi = 0$ and P_d is the diametral clearance. These values are better explained in the radial bearing with clearance illustration figure below.
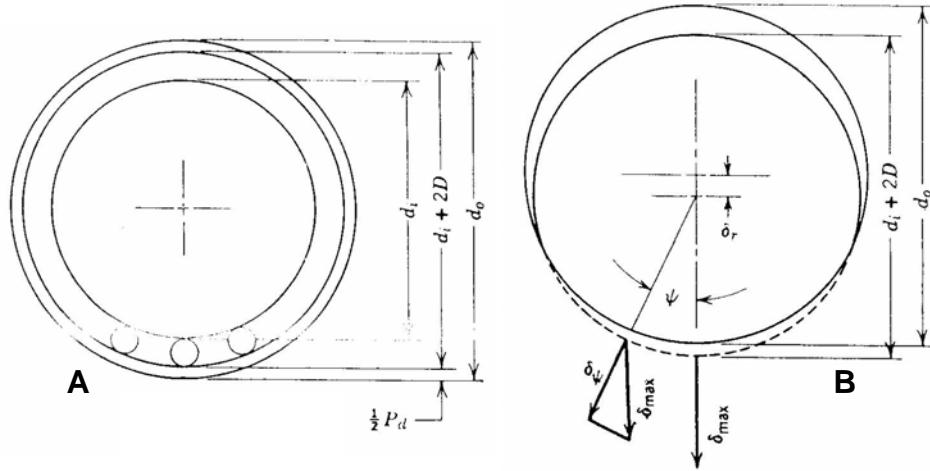
Figure 15.Radial bearing rings

Figure 15A shows the bearing before displacement occurs, and Figure 15B the bearing after radial displacement.

Equation 27 can be rearranged in terms of maximum deformation as:

$$\delta_\psi = \delta_{max}\left[1 - \frac{1}{2\varepsilon}(1 - \cos\varphi)\right] \qquad \text{Equation 28}$$

In which

$$\varepsilon = \frac{1}{2}\left(1 - \frac{P_d}{2\delta_r}\right) \qquad \text{Equation 29}$$

It is then clear by Equation 29 that the extent of the load zone is determined by the diametral clearance such that

$$\varphi_1 = \cos^{-1}\left(\frac{P_d}{2\delta_r}\right) \qquad \text{Equation 30}$$

Which yields $\varphi_1 = 90°$ for zero clearance.

From Equation 22 we can obtain Equation 31

$$\frac{Q_\varphi}{Q_{max}} = \left(\frac{\delta_\varphi}{\delta_{max}}\right)^n \qquad \text{Equation 31}$$

and by combining this equation with Equation 28 we obtain Equation 32

$$Q_\varphi = Q_{max}\left[1 - \frac{1}{2\varepsilon}(1 - \cos\varphi)\right]^n \qquad \text{Equation 32}$$

For static equilibrium to exist, the applied radial load must equal the sum of the vertical components of the rolling element loads as illustrated by Equation 33

$$F_r = \sum_{\varphi=0}^{\varphi=\pm\varphi1} Q_\varphi \cos\varphi \qquad \text{Equation 33}$$

$$F_r = Q_{max} \sum_{\varphi=0}^{\varphi=\pm\varphi1} \left[1 - \frac{1}{2\varepsilon}(1 - \cos\varphi)\right]^n \cos\varphi$$

Equation 33 can also be expressed in its integral form as shown by Equation 34

$$F_r = ZQ_{max} \times J_r(\varepsilon) \qquad \text{Equation 34}$$

where

$$J_r(\varepsilon) = \frac{1}{2\pi} \int_{-\varphi1}^{+\varphi1}\left[1 - \frac{1}{2\varepsilon}(1 - \cos\varphi)\right]^n \cos\varphi \; \partial\varphi \qquad \text{Equation 35}$$

The radial integral of Equation 35 was evaluated numerically and expressed in Table 1 below.

Table 1. Load distribution integral $J_r(e)$

E	Line Contact	E	Line Contact
0	1/Z	0.8	0.2658
0.1	0.1268	0.9	0.2628
0.2	0.1737	1.0	0.2523
0.3	0.2055	1.25	0.2078
0.4	0.2286	1.67	0.1589
0.5	0.2453	2.5	0.1075
0.6	0.2568	5.0	0.0544
0.7	0.2636	Infinity	0

From Equation 25 we obtain

$$Q_{max} = K_n \delta_{\varphi=0}^n$$ Equation 36

$$Q_{max} = K_n \left(\delta_r - \frac{1}{2} P_d \right)^n$$

Therefore,

$$F_r = ZK_n \left(\delta_r - \frac{1}{2} P_d \right)^n J_r(\varepsilon)$$ Equation 37

For a given bearing with a given clearance under a given load, Equation 37 can be solved by trial and error [8]. A value of δ_r is first assumed and ε is calculated from Equation 29 yielding $J_r(\varepsilon)$ as in Table 1. If Equation 44 does not balance, the process is repeated. This is done iteratively to find the entire load zone distribution.

Experimental Plan

The flowchart displayed in Figure 16 portrays the research plan carried out in order to measure roller skew in spherical roller bearings. All the steps presented in the flowchart are explained in detail in the subsequent parts of this thesis. The flowchart shows the overall goals and results obtained in this thesis. It should be noted that between the analysis and results stages there is an arrow pointing in both directions. This is due to the fact that at this level of the research, there was an iterative process of obtaining results and performing data analysis on the data obtained. After this process, results were validated utilizing theoretical models and/or results from work performed by other researchers in the area.
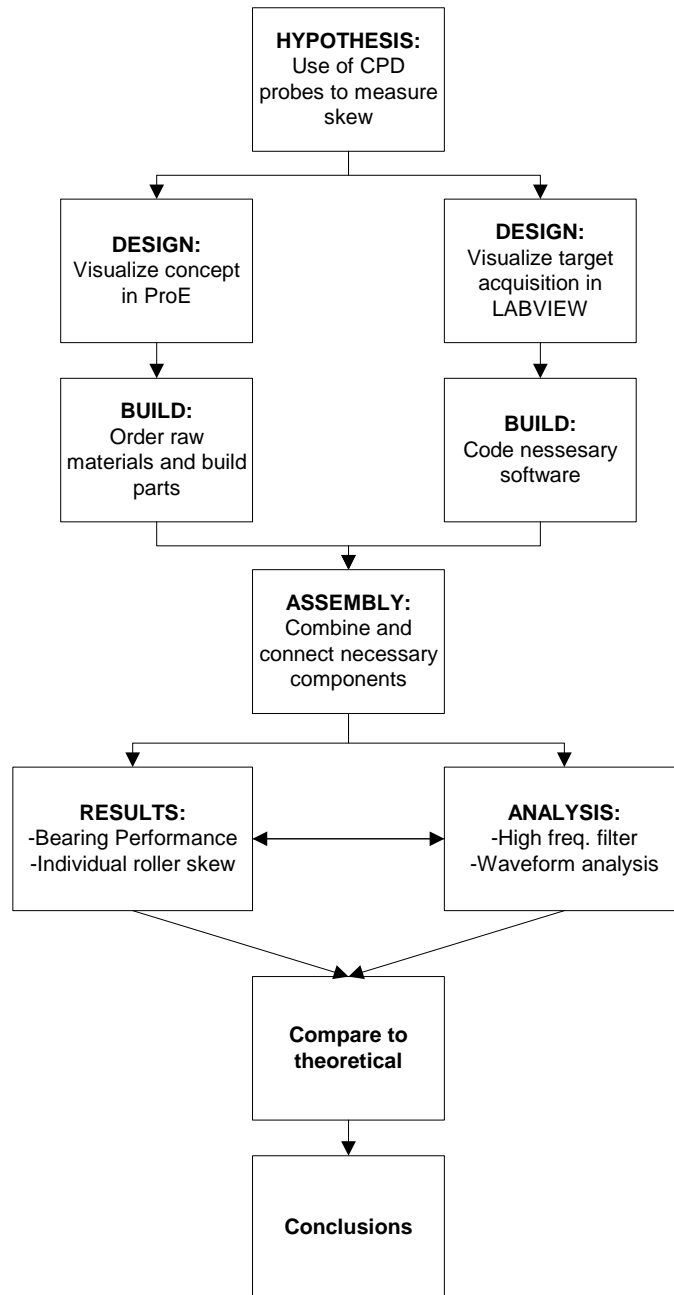
Figure 16. Experimental plan

CHAPTER 3

EXPERIMENTAL SETUP

This chapter describes the experimental setup. First, a review of the overall experimental design will be given, followed by a detailed description of the system components.

Overall System Design

A schematic diagram of the spherical roller bearing test system is shown below in Figure 17.
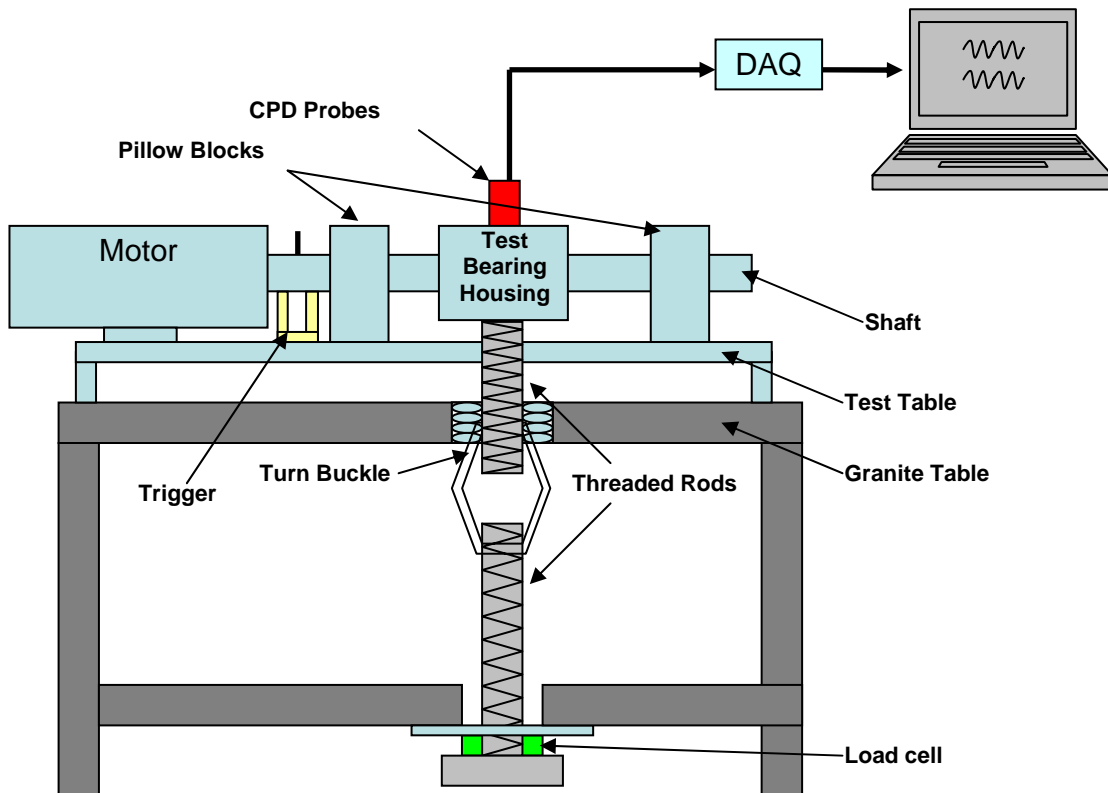

Figure 17. Bearing test schematic diagram

The setup consists of a ½ hp motor which is connected through a coupling to a stainless steel shaft. The motor and the coupling are electrically insulated from the test table and the shaft respectively to prevent any electrical noise dispersion from the motor to the probes. The shaft is supported on two ends by Torrington GYE40KRRB pillow blocks. These pillow blocks have set screws which are tightened against the shaft to prevent slipping. In between the pillow blocks, a housing which holds the test bearing is found. This housing is utilized to hold the CPD probes around the bearing, to facilitate the application of the radial load (load that is perpendicular to the shaft), and to aid in the fixation of the bearing to prevent shaft and bearing misalignment under load. The housing is connected to a loading mechanism through the granite table which provides different loading conditions for experimental purposes. The loads are recorded utilizing a capacitive load cell.

The CPD probes are arranged around the bearing housing in pairs as shown in Figure 18. The angular spacing was analytically determined by utilizing the scheme and formulas explained in the previous chapter for calculating the loading zone. This spacing was then set as part of the design parameters for this thesis; therefore it was not changed throughout all the experiments. The CPD probes needed to be placed in pairs as described by Yang, Danyluk, and Hoeprich [5] in order to obtain a phase shift between the two CPD signals and calculate skew angle based on experimental parameters.
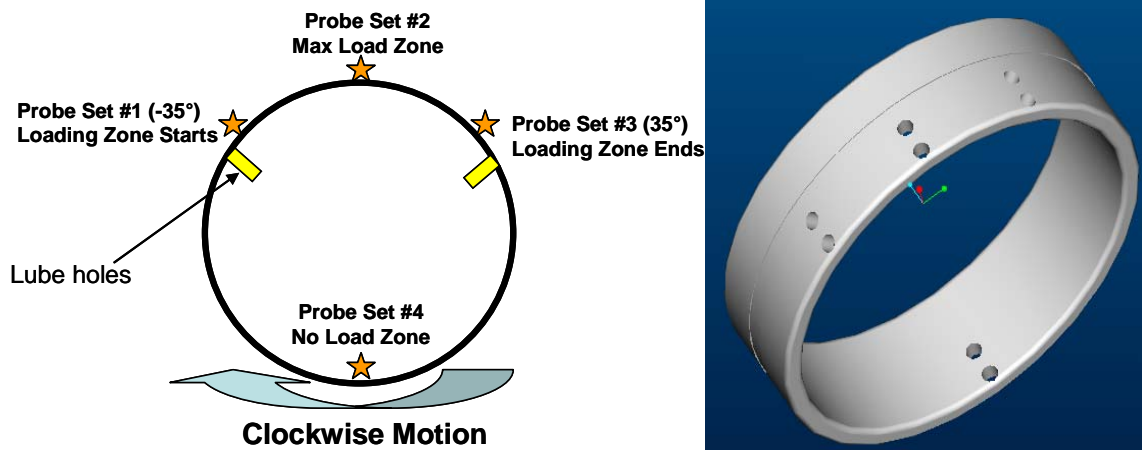
Figure 18. Probe distribution around test bearing

System Components

A graphic image of the experimental setup is shown in Figure 19 followed by an actual photograph of the system in Figure 20. The main components of the system are displayed and further explained in the subsequent parts of this section.
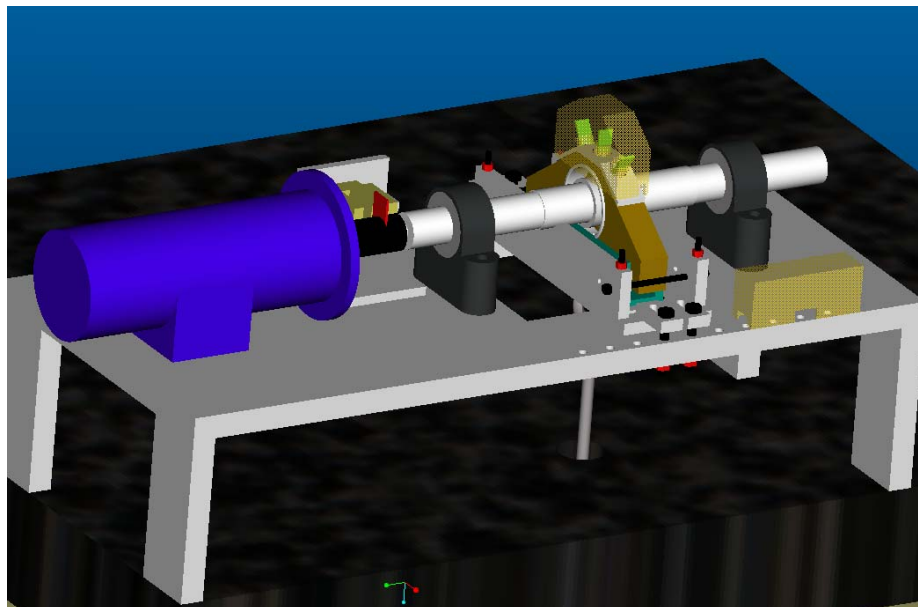

Figure 19. Experimental setup components
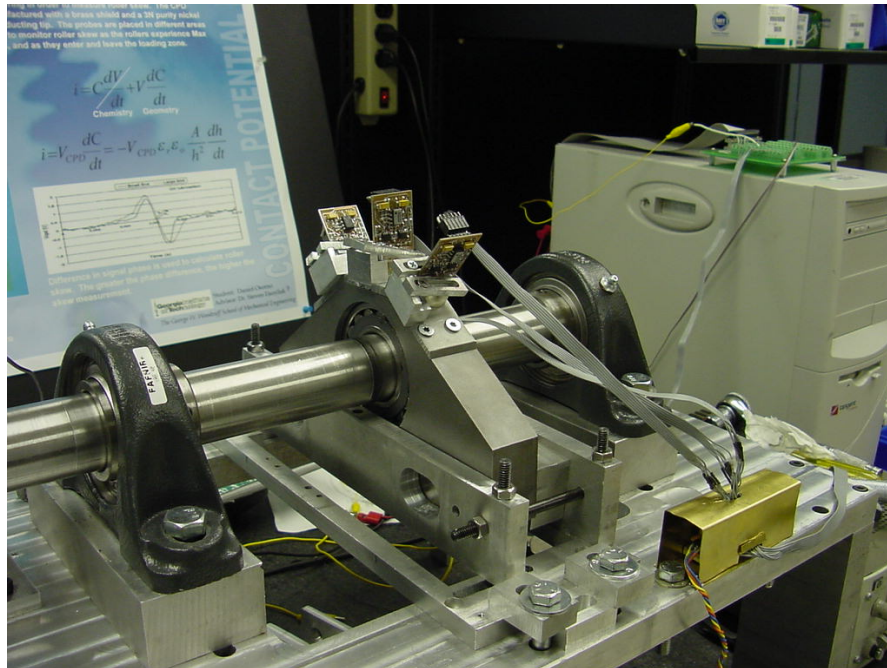
Figure 20. Experimental setup photograph

CPD Sensor Tip

Figure 21 shows the design of the probe tip which consists of a 1/32 in. brass rod surrounded by a dielectric and a metal sheath. The metal brass sheath, 1/8 in. in diameter and 0.025 in. thick, is separated from the central conducting rod by an insulating dielectric epoxy layer. This is the typical probe tip configuration utilized by the CPD research group at the Georgia Institute of Technology [15] & [16]. The shield surrounding the copper wire reduces fringe electrical fields while the epoxy dielectric serves as a spacer to maintain the shield and conducting rod separated. The conducting rod is then electrically soldered to the circuitry shown in Figure 22 while the shield is connected to a common ground. Various combinations of probe materials can be used, involving an assortment of materials and dimensions. The dimensions and materials

chosen for the experiments in this thesis were selected after various different attempts to acquire a clean signal with low signal-to-noise ratio. It should be noted that due to dimensional constraints of the test bearings, the dimension of the probe tips was also constrained.
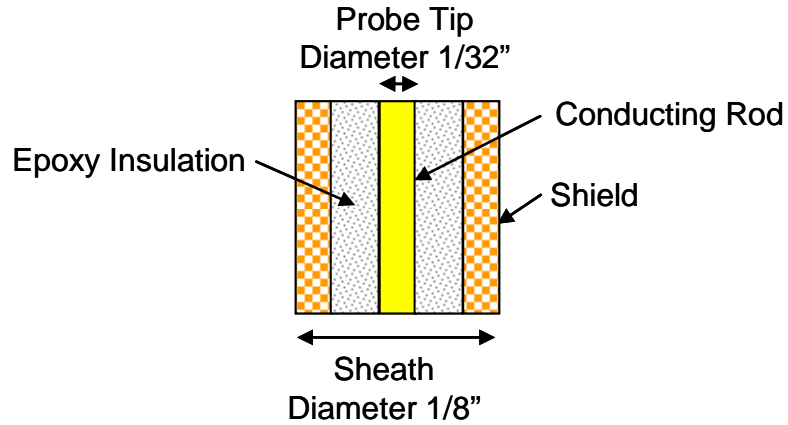

Figure 21. Schematic diagram of the cross section of the CPD probe tip.

CPD Sensor Circuitry

   Figure 22 below shows a schematic diagram of the sensor circuitry.
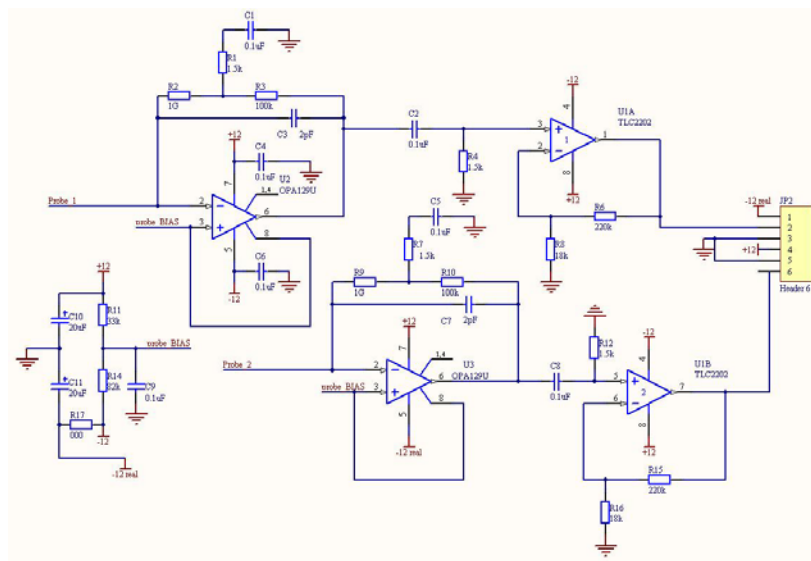
Figure 22. Circuit diagram of CPD sensor.

31

It can be observed on Figure 22 that the right side of the circuitry ends in a connector. This connector is used to supply power to the probe connect the probe to the data acquisition system. The connector legend can be found on Table 2 below.

Table 2. CPD probe connector legend

Connector #	Type	Value
1	Input	-12 V
2	Output	Probe 1
3	Input	GND
4	Input	+12 V
5	Input	GND
6	Output	Probe 2

It can also be observed on Figure 22 that there are two identical circuits wired together onto the connector. This is because both CPD amplification circuits were embedded onto the same PC board in order to simplify handling of the circuit. It was also convenient to have the pair of CPD probes connected on the same circuit board to reduce probe misalignment.

Figure 23 is part of the circuit shown in Figure 22.
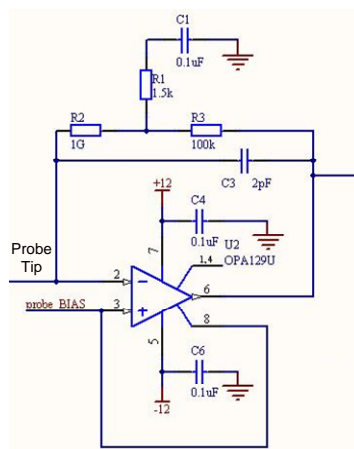
Figure 23. Current to voltage converter

From Figure 23, the lower part of this circuit is a current-to-voltage converter. Since the probe signal is a current. The upper part of this circuit is a "T-shape feedback" which consists of a loop of capacitors and resistors which are arranged to produce a very high equivalent resistance required in order to change the currents into a readable voltage.

The second part of the circuitry consists of a power amplifier as shown in Figure 24. This amplifier is utilized to increase the output signal. It should also be noted that in between the current to voltage converter and the power amplifier, there is a 100pF capacitor (labeled C2 and C8), placed to function as low band filter capacitors which aid in the reduction of noise.
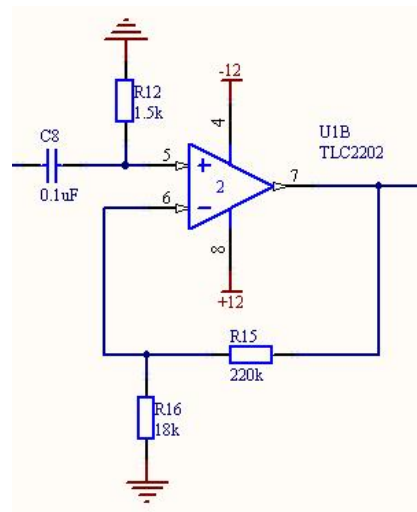

Figure 24. Power amplifier

A photograph of the actual CPD probe tips and circuitry is shown in Figure 25. The figure also shows the power amplification chips, the current to voltage converter, and all other components. It can be observed that the circuitry has a mirror line on the middle of the board, where every component found on one side is equally found on the other.

33

The back of the board is also covered in copper and serves as a common ground for the circuitry.
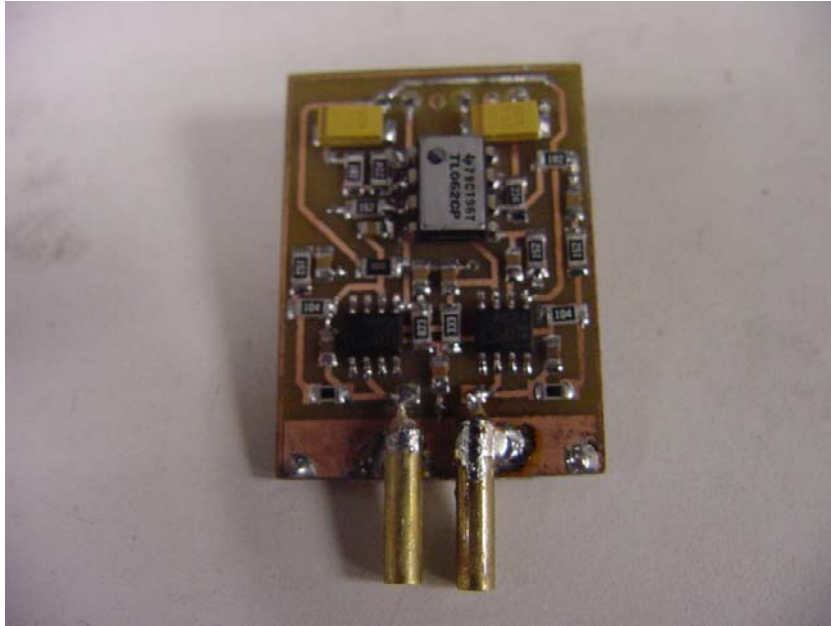
Figure 25. CPD probe and circuitry photograph

Data Acquisition System (DAQ)

The data acquisition system consists of both hardware and software. A NiDAQ 68 pin E-Series connector block and a E-Series NI 6030E Mulifunction DAQ (100kS/s, 16-bit,16 Analog Inputs) data acquisition card with analog and digital trigger serve as the main system hardware. This card has an input range of $\pm$ 0.1V to $\pm$10V and a 16-bit resolution which suffices the needs of this project [17].

The data acquisition system was set to sample at 10 kHz per channel because it is limited to a total of 100 kHz and there were 8 probes connected at a time, limiting the maximum sample rate to 12.5 kHz per channel. During the course of the data acquisition, no averaging was used since signal amplitude was not considered important for the purpose of this experiment.

The software utilized for the data acquisition was written in LabVIEW 7.1. Screenshots of the program user interface and wire diagram are displayed in Appendix A in Figure 67 and Figure 68 respectively.

Fixturing

To facilitate and improve the data acquisition process, various fixtures were machined to hold the probes in place on the bearing housing, and to hold the bearing housing against the test table.

On the first case, it was necessary to fix the probes to the bearing housing so that their position remained constant throughout the experiments. The probe tips and circuitry were placed inside polymer probe holders. These were produced by rapid prototyping (RP) so that many exact replicas could be made. The probe holders were then fixed on aluminum plates which were secured onto the top of the bearing housing. The plates were designed to be removable so that the probes could be removed to allow the mounting of a new bearing. The fixturing devices also kept the fly height between the probe tips and the roller surfaces constant so as to attempt to maintain signals in the same amplitude range [18].

On the second case, it was necessary to fix the bearing housing onto the test table to prevent the bearing housing from skewing in relation to the shaft due to the friction and torque generated. By fixing the bearing housing, it was guaranteed that the skew measurements measured by the probes were related to roller skew and not bearing skew. Figure 26 shows an exploded view of the CPD probes as they are fixed on the bearing

housing. The probe holders are then fixed to the aluminum plate using clamps as shown in Figure 27.
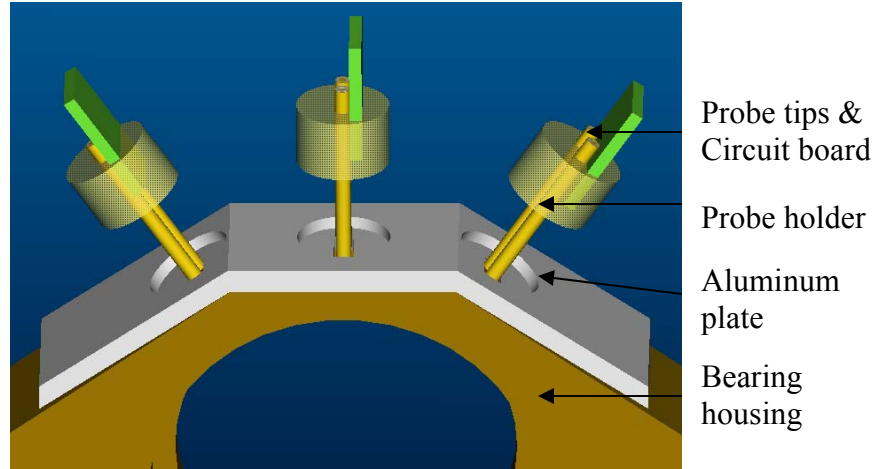

Figure 26. Exploded view of CPD probes
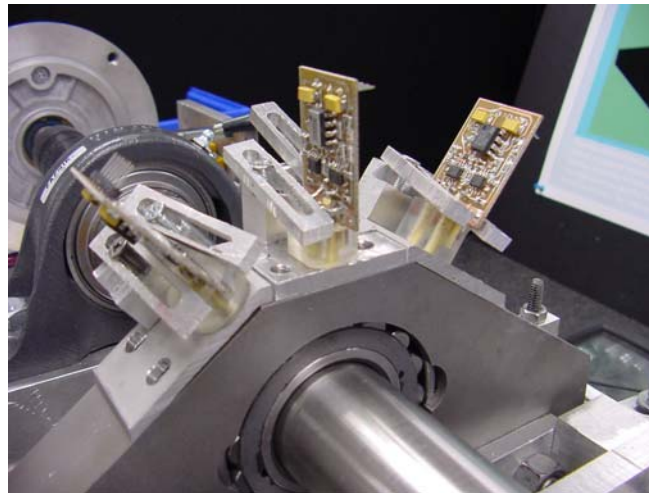
Figure 27. CPD probe fixturing photograph

Shielding

Utilizing shields was important not only during probe tip construction, but also for overall system performance. Figure 28 shows two different shields which were used to protect the CPD probes from external noise influence. The two shields were used to protect the probes on the test bearing and the connectors which distributed the power to

the probes and directed the signal from the probes to the DAQ connector block. In later chapters it will be shown how important these shields were to reduce signal to noise ratios.
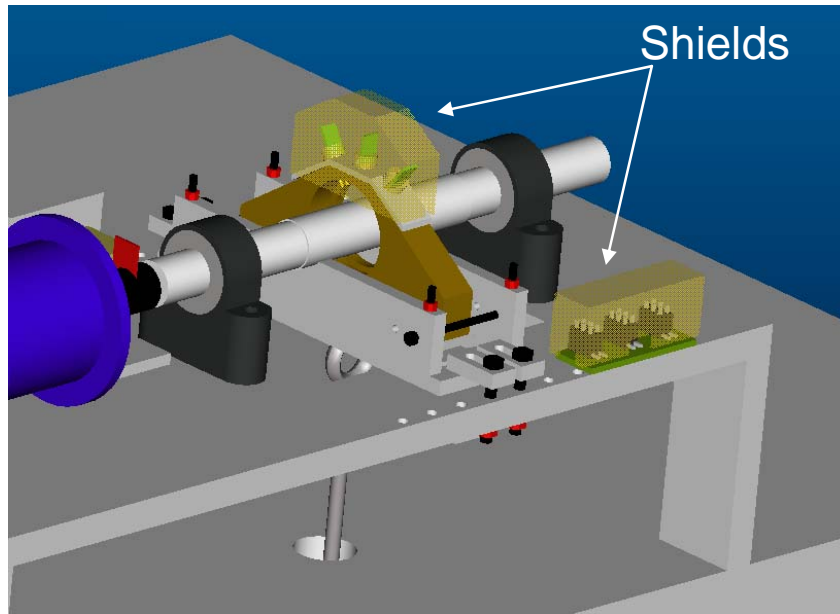

Figure 28. CPD bearing shields

Grounding

Setting a common ground for the circuitry was necessary. This ground was also used to ground the shields and the shaft via a carbon brush. Having a common ground is useful as it references all signals to the same potential. It is also a good way to discharge noise signals which are captured by the shields.

Triggering

Placing a trigger on the experimental setup was not compulsory, but aided significantly when performing data analysis.   The trigger consisted of a KFPS KP-ER-01N digital trigger mounted on an aluminum machined fixture. The trigger was placed

between the motor and the first pillow block in order to record the RPM of the shaft. The outputs of the trigger were connected to the digital trigger channels of the DAQ connector block. Unfortunately, the trigger alone was not useful for data acquisition purposes since the rollers do not rotate at the same speed as the shaft. In order to calculate the angular speed of the rollers a formula to relate the shaft speed to the roller angular speed is needed. Figure 29 shows a schematic of the rolling element rotation around the shaft.

Symbol Key		
Terms	n	rotational speed
	D	roller diameter
	α	contact angle
	d	pitch diameter
	γ	$D{*}Cos\alpha/d_m$
Subscripts	i	inner raceway
	o	outer raceway
	m	orbital motion
	R	rolling element
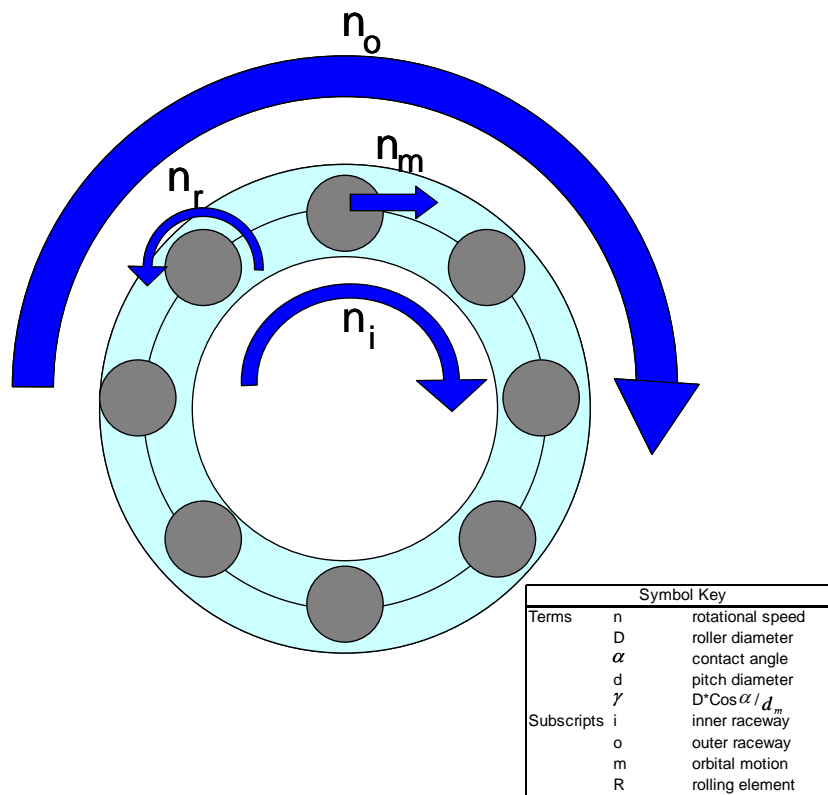
Figure 29. Rolling element rotation schematic

The rotational speed of the roller is given by Harris [8] to be:

$$n_m = \frac{1}{2}\left[n_i\left(1-\gamma\right)+n_o\left(1+\gamma\right)\right]$$
Equation 38

With the angular speed of the cage relative to the inner raceway

$$n_{mi} = n_m - n_i \qquad \text{Equation 39}$$

Assuming no gross slip at the inner raceway-roller contact, the velocity of the roller is identical to that of the raceway at the point of contact

$$\frac{1}{2}\varpi_{mi}d_m(1-\gamma) = \frac{1}{2}\varpi_R D \qquad \text{Equation 40}$$

Therefore, since n is proportional to ϖ and by substituting n_{mi} as in Equation 39,

$$n_R = \frac{1}{2}\frac{d_m}{D}(1-\gamma)(1+\gamma)(n_o - n_i) \qquad \text{Equation 41}$$

Considering only inner raceway rotation, Equation 38 and Equation 41 become

$$n_m = \frac{1}{2}\left[n_i(1-\gamma)\right] \qquad \text{Equation 42}$$

$$n_R = \frac{1}{2}\frac{d_m}{D}n_i(1-\gamma^2) \qquad \text{Equation 43}$$

Based on the geometry of the bearing, the parameters summarized on Table 2 are used to obtain γ to be

$$\gamma = D*Cos\,\alpha/d_m = 10.55/60.55 = 0.1742 \qquad \text{Equation 44}$$

Table 3. Geometrical values of Torrington 22208CJW33C4 spherical roller bearing

Description	Symbol	Value
Roller Diameter	D	10.55 mm
Cage Diameter	d_m	50+10.55 mm = 60.55 mm
Contact Angle	α	0°

From these, the orbital motion of the roller (or cage speed) is calculated to be

$$n_m = \frac{1}{2}\left[n_i\left(1 - \gamma\right)\right]$$

<div align="right">Equation 45</div>

$$n_m = \frac{1}{2} \times RPM \times (1 - 0.1742)$$

$$n_m = 0.413 \times RPM$$

Loading

The loading mechanism subjects the bearing to different radial loads. The loading mechanism consists of a variety of machined parts which connect the bearing test housing to the bottom of the granite table as seen previously on Figure 17. With the use of a turnbuckle, assortments of loads are added to the bearing. These loads are measured using a calibrated ENTRAN 2500lbs capacitive load cell. The calibration curves for the load cell are displayed in Appendix A. The regression value obtained from this curve is then manually inputted into the ENTRAN MM45 Series Sensor Monitor/Excitation to serve as a visual display of the loads being applied [19].

The design of the loading system was designed to be exceptionally flexible so that different loads could be added with ease (load being an experimental design variable).

CHAPTER 4

EXPERIMENTAL PROCEDURE

This chapter describes the overall measurement technique and the process followed to prepare for experimental data acquisition. This chapter will also provide a review of the experiments performed and steps taken during the experimental process to improve the system performance.

System Improvements

As part of the learning process for this thesis, various different improvements were completed on the system so as to improve system performance. Since some of the improvements are only significant in relation to very specific cases, only the improvements considered to be of relative importance for future CPD research are mentioned in this thesis.

Probe Tip Manufacturing

Figure 30 shows a photograph of a novel probe tip manufacturing technique developed to suffice the substantial requirement for probe tips for this experimental setup. Utilizing this manufacturing method provided plenty of long and flawless probe tips.

This technique was necessary because prior probe tip manufacturing techniques were unreliable and complicated. The new procedure allows for the assembly of numerous probe tips at a time and ensures that the conducting rod is concentric with the

shield tube (which is of important geometrical concern [18]). Concentricity was previously not ensured and was often visibly absent.
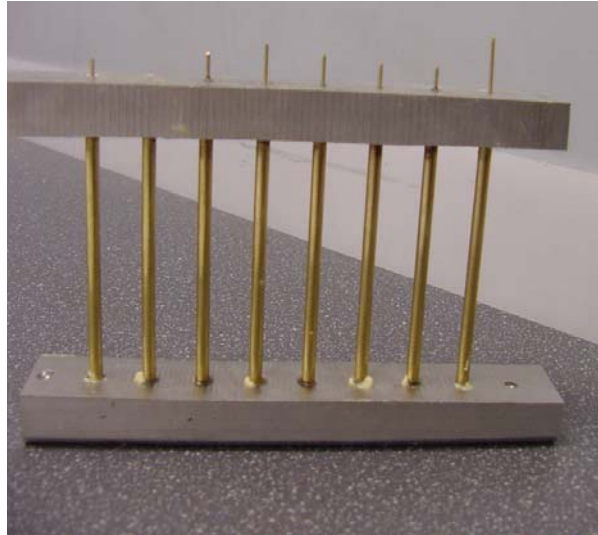
Figure 30. Novel probe tip manufacturing technique.

The novel technique consists of five steps: Drilling, cutting, assembly, pouring, and curing.

In the drilling step, a CNC milling machine was utilized to provide precision positioning which is of extreme importance in this step. A long ½ in. thick aluminum plate was clamped onto the machine and an array of equally spaced thru holes were drilled along the aluminum plate. The thru-hole diameter needed to be of the same diameter as the probe tip conducting rod, which for the purpose of these experiments was 1/32 in.. Utilizing the CNC positioning system, counter bore holes with the same diameter as the shield were drilled in the same location as the first array of holes. For the purpose of these experiments, the counter bore holes diameter was 1/8 in. After the aluminum plate has been machined, it should look similar to that of Figure 31.
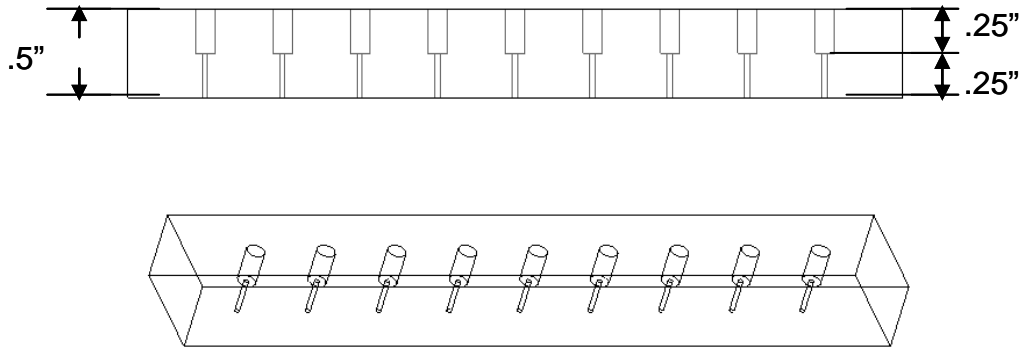
Figure 31. Probe manufacturing plate

The plate is then cut in two equal halves and these become the top and bottom plates seen previously on Figure 30.

In the cutting step, the conducting rods are cut 1½ to 2 in. longer than the probe tip length desired and the shield tubing is cut 1 to 1½ in. longer. The additional lengths are used to provide for the waste material that will be thrown away after the probes are made.

In the assembly step, the shield tubing pieces are inserted into the bottom plate allowing for the counter-bore hole to mate with one end of the tubing. Once all the shield tube pieces have been placed in their respective hole, the epoxy is poured into the tubes until full. The conductive rod is then inserted making certain that it passes the 1/32 in. hole which was originally machined through the entire aluminum plate. More epoxy is then poured into the tube to compensate for any losses incurred while inserting the conductive rod. The top plate is then inserted into the end of the shield tubing ends and the conductive rods are pushed through the top plate's thru holes. This procedure ensures that all the probe tips made have concentric holes on the top and bottom plates which are

43

utilized to provide concentricity to the probe tips. The fixture is then left to cure as directed by the epoxy instructions.

After the epoxy has dried and cured, the probe tips are cut away from the aluminum plates and these are thrown away. The tips are then ground and polished and attached to CPD circuitries to complete the probe.

Circuitry Design

During the course of this thesis, three different probe designs were developed and experimented. Each design improved the previous design in order to more effectively cope with the objectives of the thesis. The first probe circuitry design is displayed in Figure 32. This was a simple probe design which was of the same type of circuits used before by the CPD group in the Electronic Materials Research Lab at Georgia Tech. For the purpose of this thesis, the 1Gohm resistor was incorporated to provide a higher gain for the circuit amplification stage.
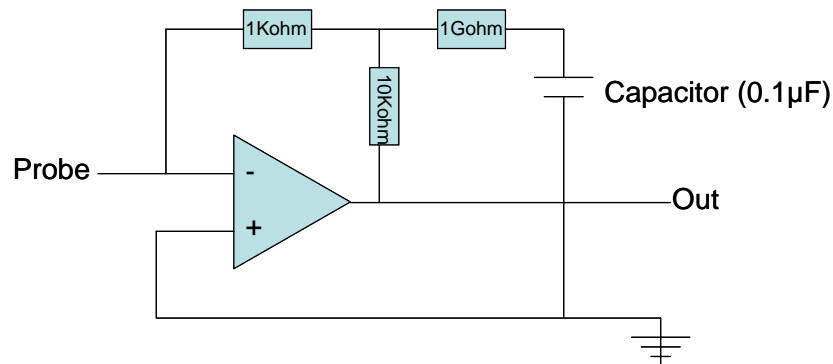
Figure 32. CPD Bearing probe circuitry ver1.

The second probe circuitry design attempted to correct a problem encountered with positioning. Since a pair of probes was needed in each probing location, and the first set of probes constructed for the experiments were individually positioned, there was excessive variability between the spacing of the probes. The second version of the probe circuitry combined a pair of probes under the same amplification chip in order to construct the pair of probes as a single unit. The design also combined input power and ground lines to reduce the number of connector pins that were connected to the circuit board. Figure 33 below shows a schematic diagram of the second probe circuitry version developed for this thesis.
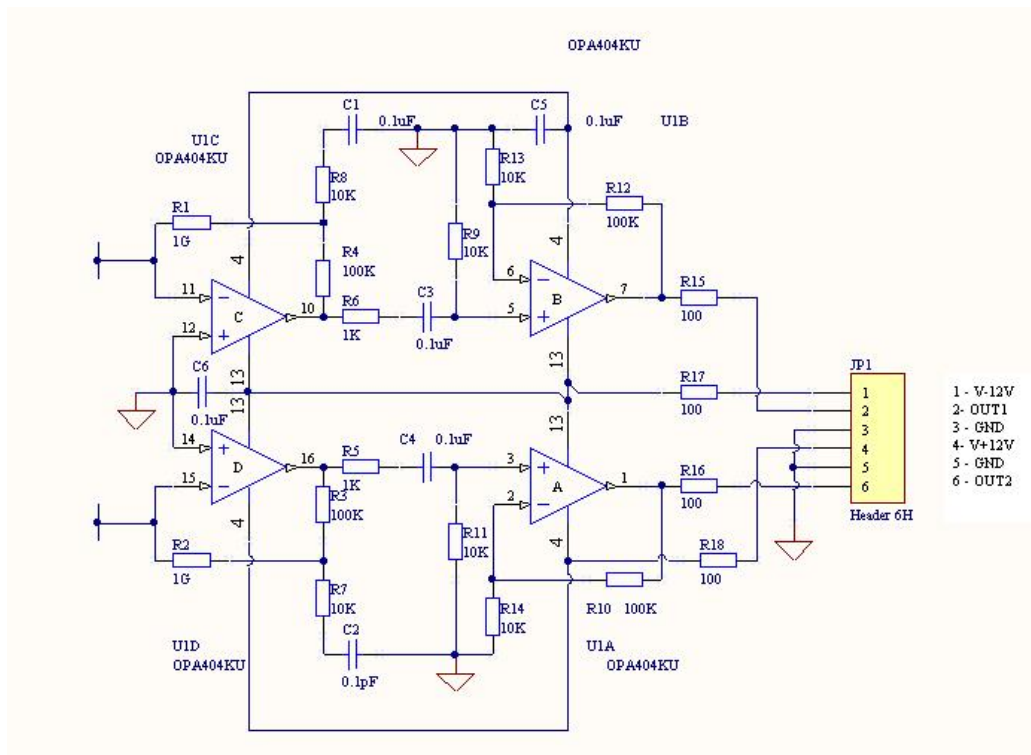
Figure 33. CPD Bearing probe circuitry ver2.

The third probe circuitry design developed for this thesis incorporated the same principles of found in the second version probe, with an addition of a 5V bias voltage applied to the probe tip in order to acquire cleaner and stronger signals from the roller motion. The third probe circuitry design is shown in Figure 22. It should be noted that the connector pins for the third probe design were designed with the exact same inputs and outputs. Due to this design constraint, it was necessary to draw the 5V differential bias for the probe tip from the original -12V and +12V supplied by the power supply. In order to accomplish this bias, the circuitry shown in Figure 34 was developed.
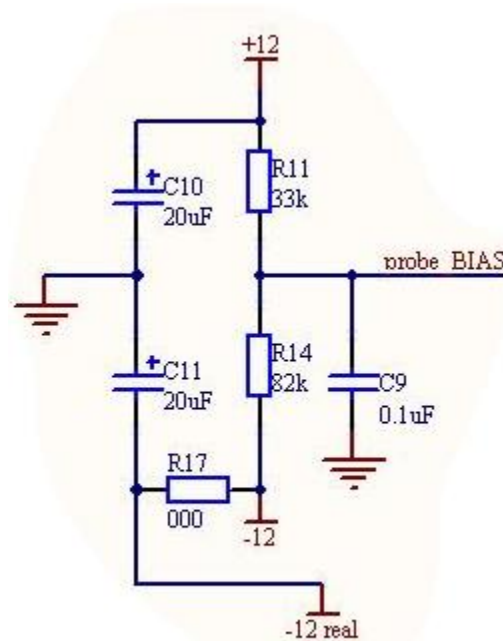
Figure 34. CPD probe bias

Circuitry Manufacturing

During the course of this thesis work, not only were different probe designs utilized, but the way that the probe circuitries were manufactured was also improved.

46

Unlike previous versions of CPD probes, the probes built for this thesis consisted entirely of surface mounted components. This change in materials allowed for the miniaturization of the probe circuitry and the availability of high end components at low costs. Since all the components used were surface mount, new circuit board manufacturing techniques were required in order to provide the backbone of the circuit. No wires were utilized in the making of the probes; all connections were embedded directly onto the circuit board. The software package Altium DXP 2004 was utilized to create the circuit board designs. This software allowed the user to input the type of component and according to their size, the software would accommodate the required spacing in order to provide accurate soldering.

Once the circuit board designs were finalized, the mirror of this image would be printed onto a transparency using a regular computer laser printer. The transparency with the mirror image printed on it would serve as a mask for the development of the design onto a copper PC board. The type of photo resist needed for the development onto the copper film is an important consideration. Depending on the printed design, it is desirable to use either positive or negative resist to build a layer of photo resist on the copper. Once the photo resist was developed by a light bulb, the PC board would be taken to a bath of copper etching solution to strip away undesired copper and leave room for connection paths. These connection paths replace connection wires and allow for the necessary spacing to solder the surface mount components needed to complete the circuit.

Learning basic and intermediate soldering techniques/principles was of utter importance for the accomplishment of this project [20].

System Preparation

In order to start experiments, some routine exercises needed to be done, some more often than others, to prepare the system in order to run experiments. These steps are described in this section.

Mounting

Mounting the bearing onto the steel test housing is a very important procedure to ensure that the probes will adequately fit in their respective positions (as shown in Figure 18) and to guarantee that the bearing will not be displaced during the experimental phase due to forces induced to it by the shaft's rotation. A tight fit was required between the bearing's outer raceway and the test housing's machined counter bore hole designed to hold the bearing because of high speeds and high loads parameters. The tight fits were achieved by pressing the shaft into the bearing and the bearing into the test housing bore. Because a press was used, particular care had to be taken in the dimensioning and tolerancing of the mating parts.

Based on the fitting practice tables for a tight fit for spherical roller bearings [7] for the 22208CJW33C4 spherical roller bearing with an OD of 80 mm, a 13 μm to 45 μm tight fit is necessary. The bearing tolerance is +0 μm to -13 μm, so the housing bore was milled to (79.974 +/- 0.009 mm). This was done with tight squareness and minimal out of round as specified.

Once the parts were properly machined, a proper mounting scheme was considered to ease the mounting of bearings onto the housing as well as to reduce the

number of mounting tools needed for the experiment. Figure 35 and Figure 36 show the

tooling needed for assembly of the shaft, bearing, and test housing.
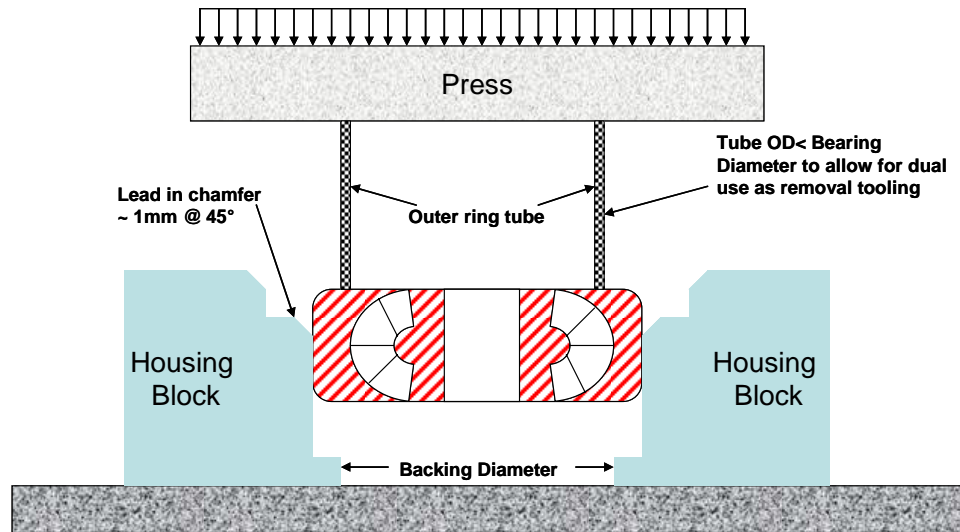
Figure 35. Assembly tooling 1
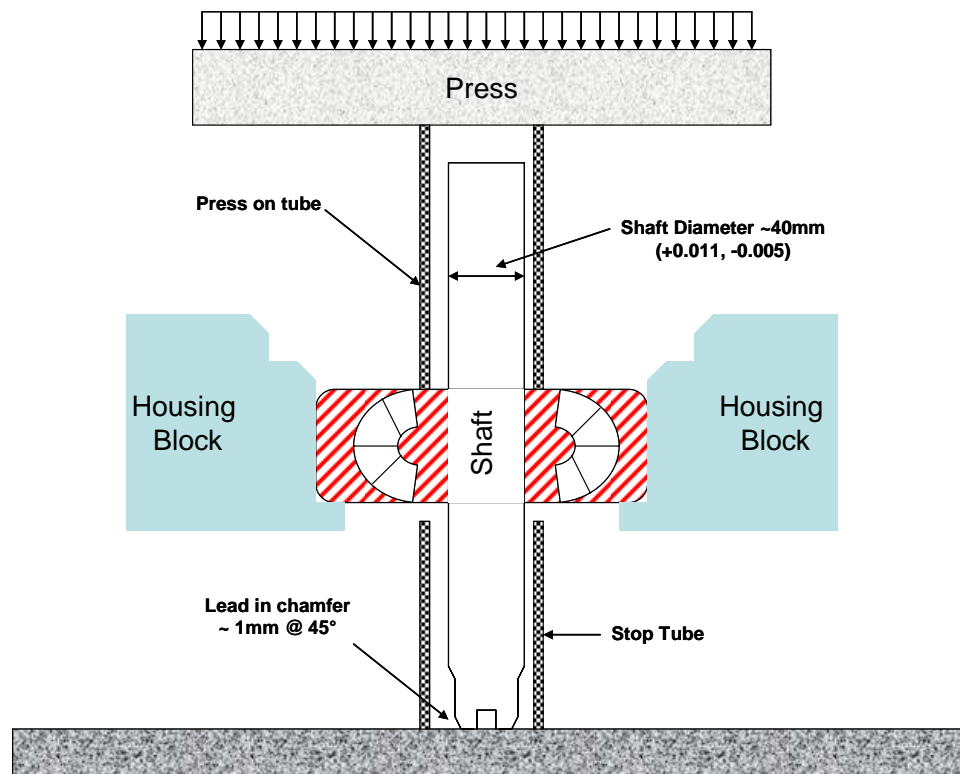
Figure 36. Assembly tooling 2

Figure 37 and Figure 38 below show the tooling and procedure necessary to remove the bearing from the housing and from the shaft.
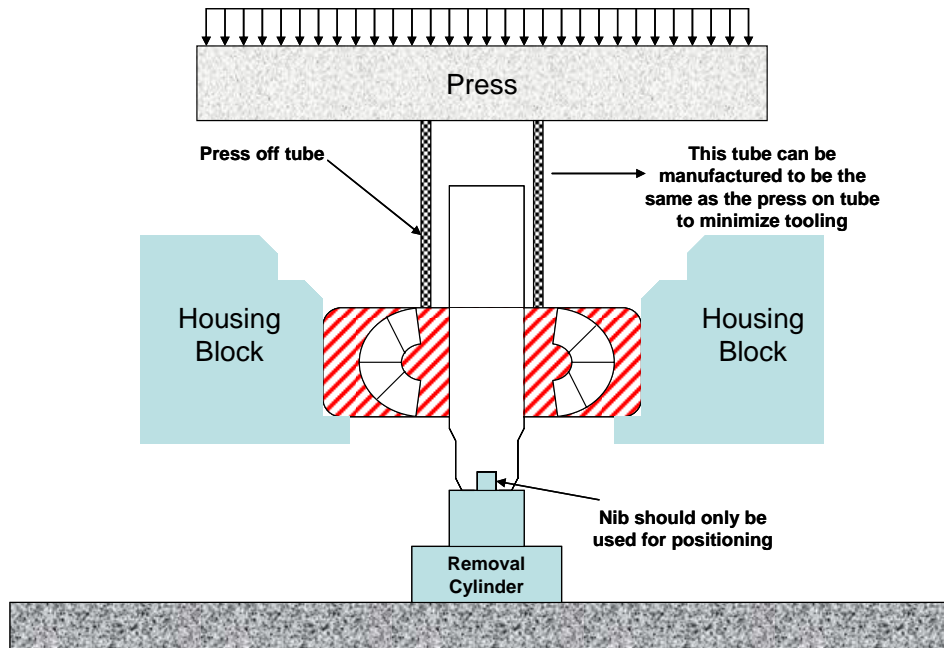
**Figure 37. Disassembly tooling 1**
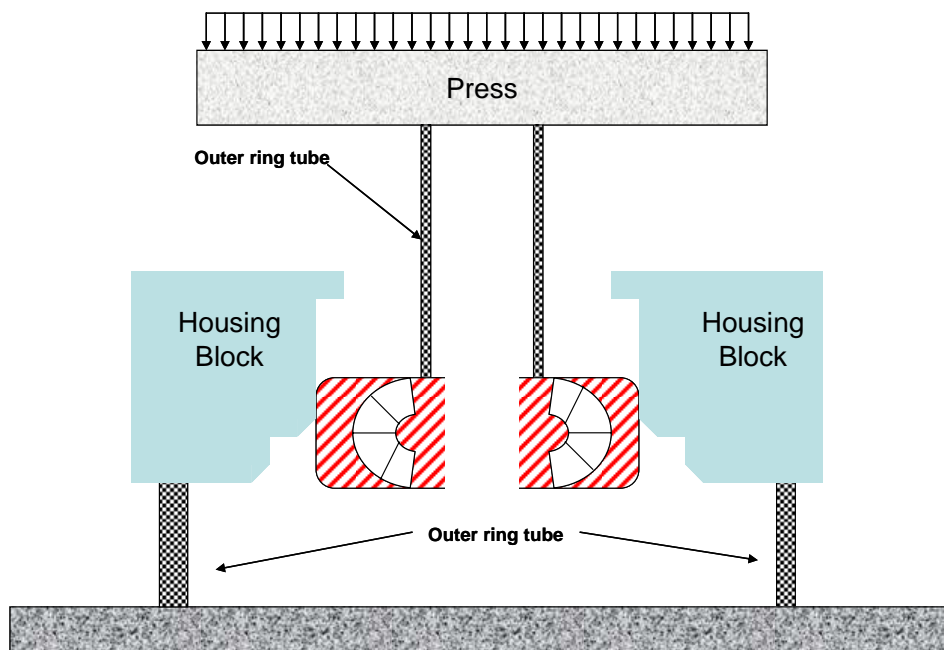
Figure 38. Disassembly tooling 2

By utilizing this assembly and disassembly scheme, the tooling needed is reduced. A summary of the parts needed for this procedure is described in Table 4.

Table 4. Assembly/Disassembly parts summary

Part #	Tool	Use
1	Loading/removal innner tube	Assembly/Disassembly
2	Press on tube	Assembly/Disassembly
3	Stop tube	Assembly
4	Removal cylinder	Disassembly
5	Housing tube	Disassembly

Greasing

Prior to running experiments, it is necessary to lubricate the bearings. In order to maintain the rolling bearing's anti-friction characteristics, lubrication is needed to minimize rolling resistance due to the deformation of the rolling elements and raceway under load, and to minimize sliding friction occurring between rolling elements, raceways, and cage.

As per exchanged emails with Timken Representative Mike Kotzalas [21], usual greasing practices suggest packing the bearing at least ¾ full of grease. In order to accomplish this task, a syringe with a plastic tapered needle was utilized to inject Timken Premium Mill Grease (ISO VG 460 with a VI of 95) into the allowed spaces. Re-greasing was necessary only after exchanging bearings.

Acquisition Parameters

After the experimental hardware was setup, it was necessary to adjust the acquisition parameters in accordance to the experiments to be run and the results desired.

The three important parameters related to the data acquisition process were shaft speed, number of samples to acquire, and the scan rate.

The shaft speed is controlled by the variable power input knob of the motor, and measured by the KFPS KP-ER-01N digital trigger. The number of samples and scan rate are controlled by the LABVIEW software created. By correctly manipulating these variables prior to running experiments, it is possible converge faster to the target data in the data processing stage.

A sample experiment planning model is displayed in Table 5 below. The variables are displayed at the top with yellow background, the calculations are displayed in the middle with light blue background, and the results are displayed at the bottom with pink background.

Table 5. Experiment planning model

600	RPM
68000	Samples
55000	Scan Rate
10	RPS
0.412882	rev/RPM
4.12882	rev/sec
16	Rollers
66.06112	Rollers/Sec
1.81818E-05	sec/sample
1.236363636	sec
81.67556655	PEAKS

For this specific experiment, the shaft revolution was 600 RPM and the data acquisition parameters of 68,000 samples and 55,000 samples per second scan rate were used.

The revolutions per second (RPS) are calculated by using Equation 46 below.

$$RPS = \frac{RPM}{60}$$
<div align="right">Equation 46</div>

The revolutions of the cage per RPM of the shaft were previously calculated in Equation 45. With this value and the RPS it is possible to calculate the revolutions experienced by the rollers per second as shown in Equation 47.

$$\frac{rev_{cage}}{sec} = RPS \times 0.412882$$
<div align="right">Equation 47</div>

By multiplying the revolutions of the cage per second to the number of rollers in the bearing, it is possible to calculate the rollers that pass by a probe every second as shown by Equation 48.

$$\frac{Rollers}{sec} = \frac{rev_{cage}}{sec} \times 16$$
<div align="right">Equation 48</div>

The acquisition period is obtained by obtaining the inverse of the scan rate as shown below

$$Acq.Period(\frac{sec}{sample}) = \frac{1}{ScanRate}$$
<div align="right">Equation 49</div>

and the time in seconds of data that will be measured during the experiment is calculated in Equation 50.

$$Time = Sample \times \frac{sec}{sample}$$
<div align="right">Equation 50</div>

With the time of acquisition and the number of rollers that pass each probe per second, it is then easy to calculate how many rollers will pass the probe during the acquisition period as described by Equation 51.

$$\frac{Rollers}{sample} = \frac{Rollers}{sec} \times \frac{sec}{sample}$$
<div align="right">Equation 51</div>

By knowing in advance the quantity of rollers that will pass the probe prior to starting the experiment, it is possible to plan the experiment for a certain measurement. In the case exemplified in Table 5 the target was to measure 80 rollers (5 revolutions per each individual roller) at a desired 55,000 scans/sec rate. Therefore, approximately 68,000 samples are needed to obtain a little over 80 peaks. As it can be observed, it was sometimes useful to overshoot the number of revolutions needed just in case the accuracy of the RPM of the shaft was off.

Measurement Technique and Post-Processing

After the acquisition parameters are set, and all wires are connected to the proper probe, the power supply is turned on to provide power to the probes. The probe's protecting shield is then set in place to reduce the signal-to-noise ratio The shaft is turned on and a few seconds after, when the trigger displays the correct RPM (since it takes the motor about 2 seconds to achieve the desired speed) the data acquisition software is turned on. If the data is to be recorded, it is necessary to activate the "Write File" control and set the path of the file to be written. After the data has been acquired, it is recorded as a text file and transferred to a faster processing computer to perform data processing and post-analysis.

The text file is filtered using the Matlab programs shown in Appendix A. Each program corresponds to a different measurement depending on the amount of channels being probed during the experiment. If only a single pair of probes is being measured, the resolution of the measurements can be increased up to 55,000 scans per second. Likewise, if all 8 probes are being measured, the resolution needs to be decreased to

about 12,500 scans per second (this limiting factor is due to the maximum resolution of the data acquisition card). The amount of probes to be tested at a time depends on the target set for the experiment. If the target is to see overall bearing performance, all 8 probes are required to obtain measurements from all locations of the loading zone. If the target is to evaluate the behavior of the rollers at a single measurement location, then a single pair of probes can be measured, thus increasing the resolution.

The filter used for the data is a pre-analysis filter used to reduce high frequency noise which is embedded onto the signal waveform. The filter utilizes the box-car filtering technique [22] with a narrow window size in order to affect the original data as least as possible. Comparison waveforms of a sample raw data obtained by LABVIEW and the filtered data of the same waveform are displayed in Figure 39 and Figure 40.
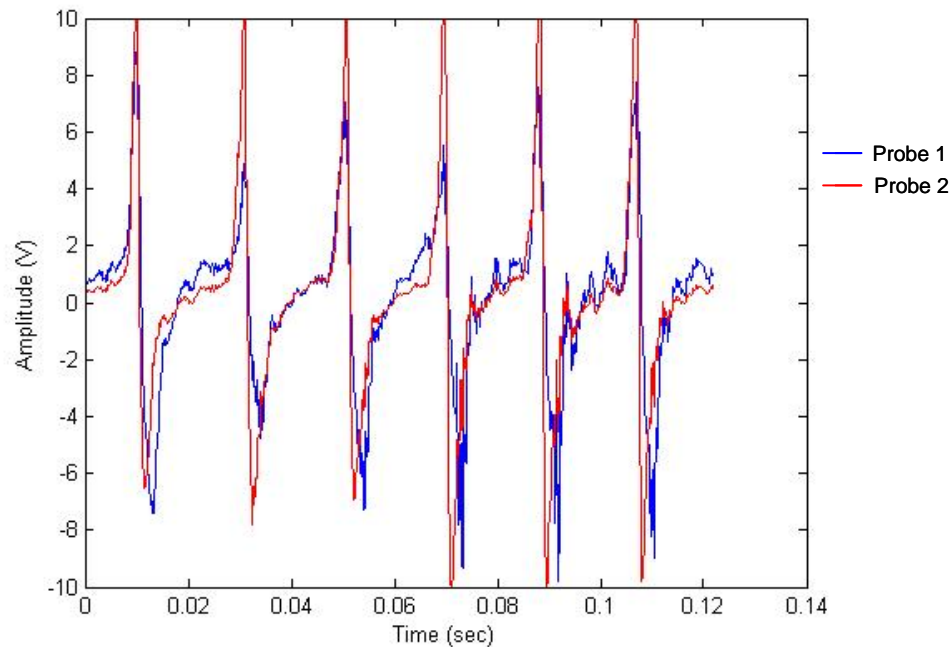
Figure 39. Raw unfiltered data
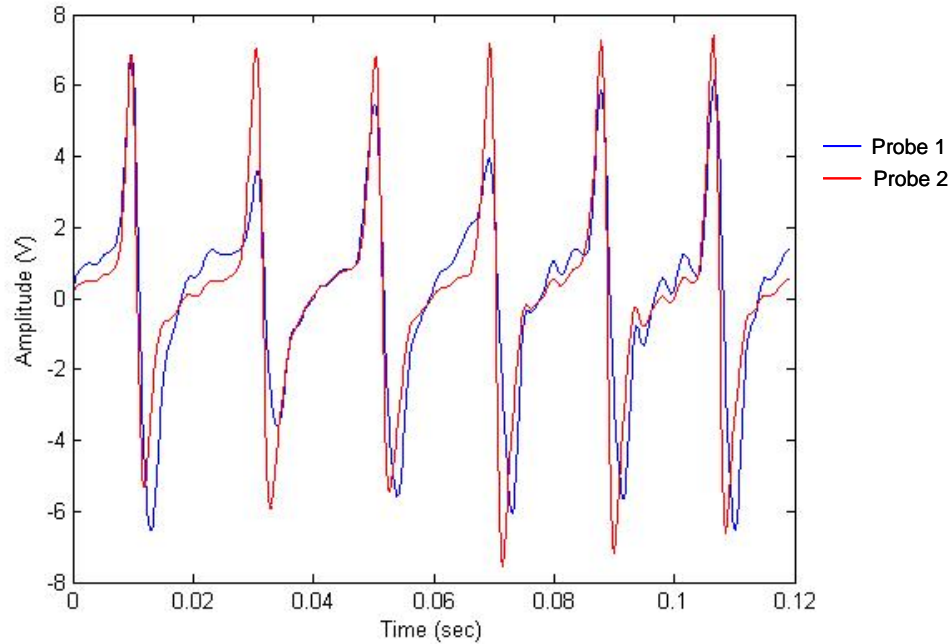
Figure 40. Box-car filtered data

As it can be observed, the box-car technique reduces high frequency noise while maintaining the waveform's integrity for further processing.

Once the data has been filtered, an Excel spreadsheet is created compiling all the sets of measurements made for a certain experiment. A custom Excel template was created and pasted into each filtered data spreadsheet to minimize the effort in data processing. A sample of the template is displayed in Figure 41. The spreadsheet template displayed in Figure 41 was used to process the data of three pairs of probes. Column A displays the time array of the experiment, and columns B to G display the corresponding amplitude values for each individual probe. Up to column G the data given by LABVIEW which is then filtered using Matlab can be found. Columns H to AD contain the information pasted as a template in order to aid in the data processing procedure. Columns J to T detect for each channel whether the signal has crossed the zero amplitude line going from a positive value to a negative value.

Figure 41. Excel template sample

Figure 42 below displays a typical sample of data that the template attempts to process. The data displayed in Figure 42 corresponds to the signature waveform of a single roller for two probes. The difference in amplitude of the signals is due to the difference in probe fly height with respect to the roller surface. This difference is not important since the value sought for is a time value and not amplitude. The Excel template attempts to find the phase difference in units of time of the two signals for every roller. In order to do this, it finds the place in each roller waveform where after passing the maximum positive peak it passes through the x-axis (zero amplitude line) in order to get to the minimum negative peak. As it can be seen in Figure 42, this point occurs at about 0.018 sec for both probes.
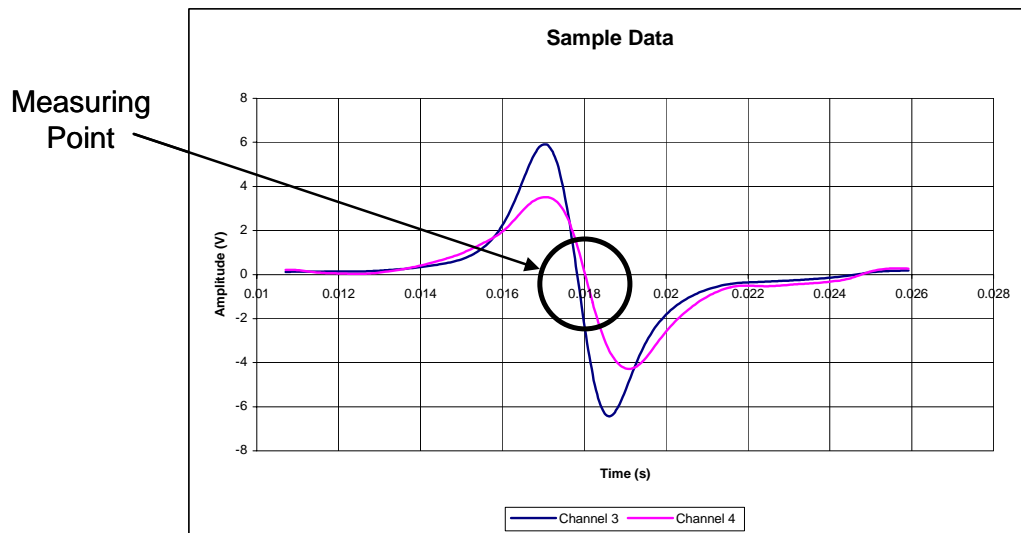
Figure 42. Sample roller data

The Excel template obtains the x-intercept for each probe's waveform and calculates the phase difference between a set of probes by calculating the difference in time at which the signals cross the x-axis.

In an ideal case, all waveforms would have a similar shape as the one seen on Figure 42. If this was the case, the data processing process would be extremely simple and short. Unfortunately as seen on Figure 43, there are waveforms that contain fluctuations due to vibrations or grease displacements within the bearing and this results in false signals. These fluctuations would be seen by the template as points in a waveform which traverse from positive to negative crossing the x-axis and would give a false location of a measuring point.
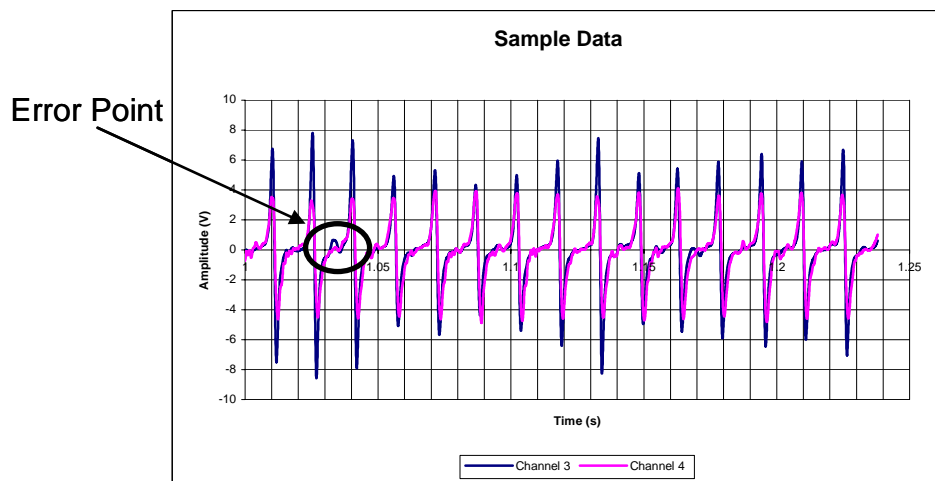
Figure 43. 15 Roller sample data

In order to reduce this type of error, thresholds are defined in the Excel template (cells V2:AA3) for the maximum and minimum peaks respectively expected prior to the measuring point. These thresholds instruct the software to look for measuring points that are generated by a maximum peak greater in magnitude than the threshold set for the positive peak, and by a minimum peak greater in magnitude than the threshold set for the negative peak. This step considerately reduces the work needed in the inspection process that follows.

After the Excel template has recognized measurement points that coincide with the criteria required, an inspection process is required to make sure that the software has cleaned all the misleading data generated by imperfections.

The last part of the Excel template, columns V to AD, collects the measurement points of every set of waveforms, calculates the phase differences, and organizes the information for plotting purposes.

This measurement technique and post-processing process is of absolute importance for the successful measurement of skew for the spherical roller bearings since a mistake can throw off the results. This process is also the most time consuming part of a routine experiment.

Roller Skew Calculation

After a phase difference between two signals is obtained from the Excel template, it is necessary to transform it into skew. This is done by implementing geometrical formulas derived from Figure 44. In this figure it is observed that as a skewed roller passes the surface of the CPD probes, there should be a time delay between the signals generated by each probe due to the fact that the surface of the roller passes one probe prior to the other one. The time delay is then captured by the DAQ and recognized as a phase shift between the two signals. This phase shift is then used along with the geometry of Figure 44 to calculate skew angle in degrees.
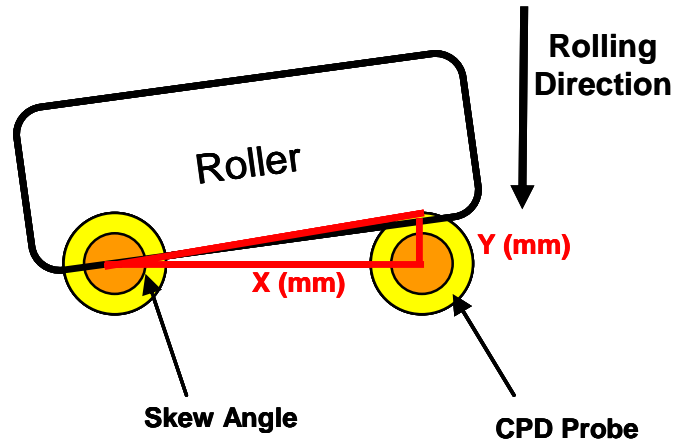
Figure 44. Roller skew schematic

Table 6 below displays a sample transformation performed for a set of probes to calculate the skew angle from the signals. The variables are displayed at the top with yellow background, the calculations are displayed in the middle with light blue background, and the results are displayed at the bottom with pink background.

Table 6. Phase-to-Skew sample transformation

600	RPM
0.00018	Delta T
10	RPS
0.412882	rev/RPM
4.12882	rev/sec
16	Rollers
35.4	Outer Radius(mm)
222.4247599	Circumference (mm)
918.3517971	speed (mm/sec)
0.222	Probe Spacing (in)
25.4	in to mm
5.6388	Probe Spacing (mm)
5.6388	X (mm)
0.165303323	Y (mm)
0.029306944	SKEW ANGLE (radians)
1.679164189	SKEW ANGLE (°)

61

For this specific experiment, the shaft revolution was planned to be 600 RPM and the phase difference between two probes was found to be 180 μ sec. The revolutions per second (RPS) of the shaft were calculated previously utilizing Equation 46. Likewise, the revolutions of the cage per RPM of the shaft were previously calculated in Equation 45 and the revolutions experienced by the rollers per second in Equation 47. The outer radius of the surface of the roller is calculated using Figure 8 to be 35.4mm. The circumference of the outer surface of the roller is then calculated in Equation 52.

$$Circum_{Outer} = 2 \times \pi \times Radius_{Outer}$$
<div align="right">Equation 52</div>

The angular speed at this point is then calculated in Equation 53.

$$Speed_{Angular} = Circum_{Outer} \times \frac{rev}{\sec}$$
<div align="right">Equation 53</div>

The spacing between the centers of the probes is used as the X component of the triangle in Figure 44. The Y component is calculated by multiplying the angular speed by the phase difference (in seconds) calculated by the Excel template as displayed in Equation 54.

$$Y_{comp} = Speed_{Angular} \times time$$
<div align="right">Equation 54</div>

Once both the X and Y components now known, the skew angle is calculated as shown by Equation 55.

$$\theta_{deg} = Tan^{-1}\left(\frac{Y}{X}\right)$$
<div align="right">Equation 55</div>

Experiments Performed

   The experiments performed varied in length and objective. At first, overall bearing performance was expected to be calculated but after performing preliminary data analysis it was observed that individual roller measurements could also be obtained. The list of experiments performed is discussed in the next chapter. These experiments were performed at different shaft speeds and radial load conditions.

CHAPTER 5

RESULTS

This chapter describes the experimental results. Various experiments were carried out in order to validate and ensure system performance, while other experiments were targeted towards acquiring information about the behavior of the bearing and rollers at certain conditions.

CPD Dependence on Frequency

It was seen that the amplitude of the CPD signal read by the data acquisition software varied in amplitude depending on the frequency of consecutive measurements. Experiments were performed using all the CPD probes and circuitries built in order to characterize each probe. A plot of the frequency response from each probe at a 100 micron fly height is displayed in Figure 45 below. In this figure it can be observed that there exists a constant gain region for all probes between 100 Hz and 1000 Hz. This region constant gain region sets the limits for the orbital speed of the rollers since it is ideal to take measurements in this region to avoid data fluctuations due to probe frequency response. In Figure 45 it can also be observed that the frequency range (red) utilized for the experiments was limited due to the limited speed constraints of the motor.

After the plot was obtained, based on similar gain values, CPD probes were designated a specific number which identified their location around the test housing. The objective was to match each pair of probes so that the gain between both probes was similar. Matching two probes with similar gains would ease data visualization since

theoretically they should produce similar waveforms with similar amplitudes. The location of each probe around the bearing housing is displayed by Figure 46.
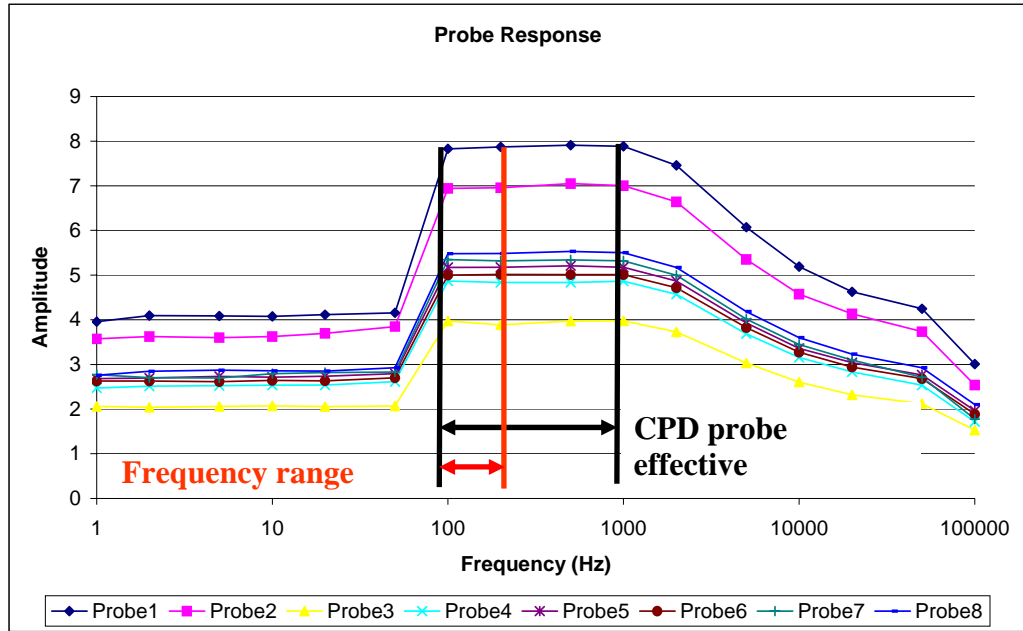
Figure 45. CPD probe response
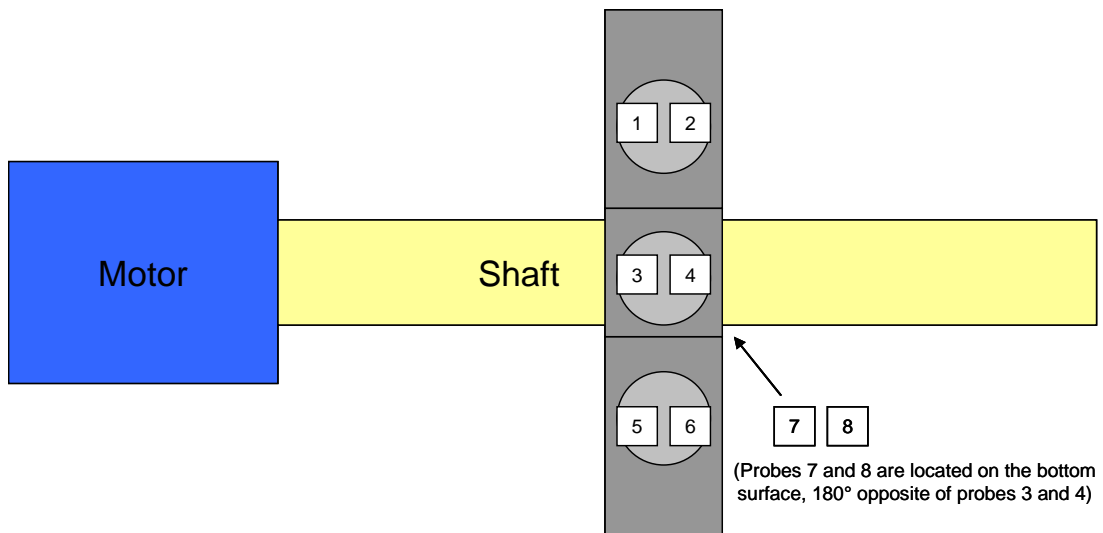
Figure 46. CPD probe location

Missing Roller Experiment

After removing a roller from the test bearing, a scan of the bearing (16 rollers) was taken using all the probe locations shown in Figure 46. The results in Figure 47 to Figure 50 show the spectrum of the bearing for an entire revolution as seen from each location. This experiment is performed as a proof of concept in order to test whether the CPD probes can detect a flaw in the rollers of a bearing, in this case, a roller missing. The results obtained correlate with the expected generated signal. By removing a roller, a large fly height is introduced between the probes and the cage which produces a flat response of zero amplitude. This experiment also serves the purpose of showing how much time it takes for the missing roller to move from one probe location to the other. This information is useful to calculate experimental roller orbital speeds or to measure lag/lead of the rollers at different parts of the bearing loading zone.
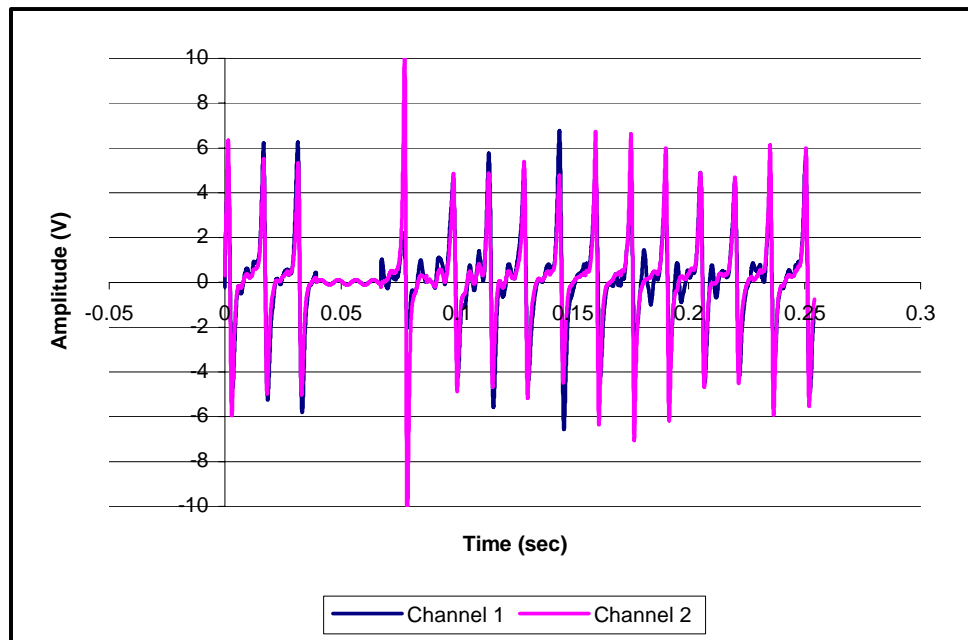
Figure 47. Missing roller probe 1-2
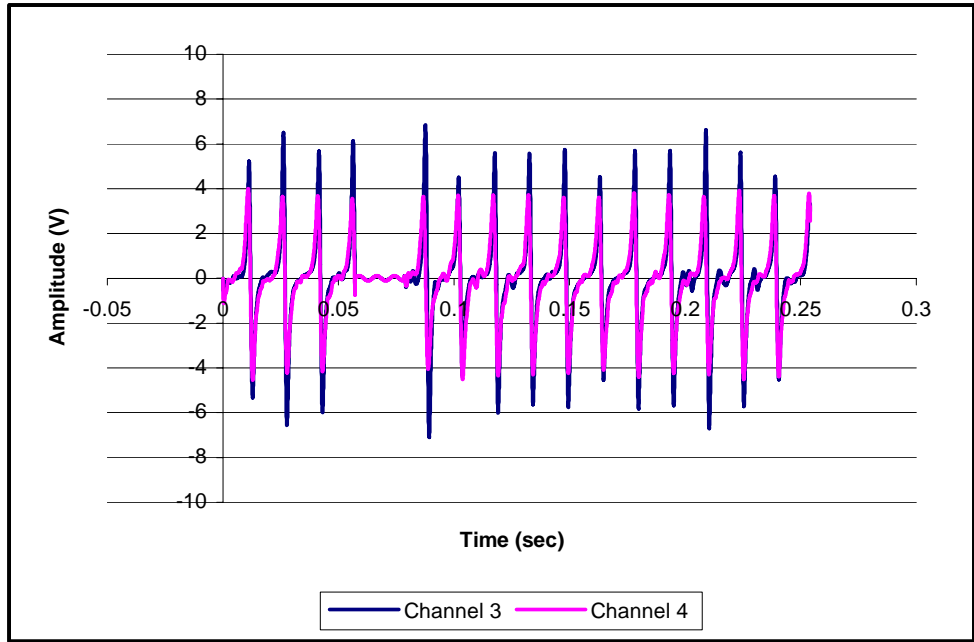
Figure 48. Missing roller probe 3-4
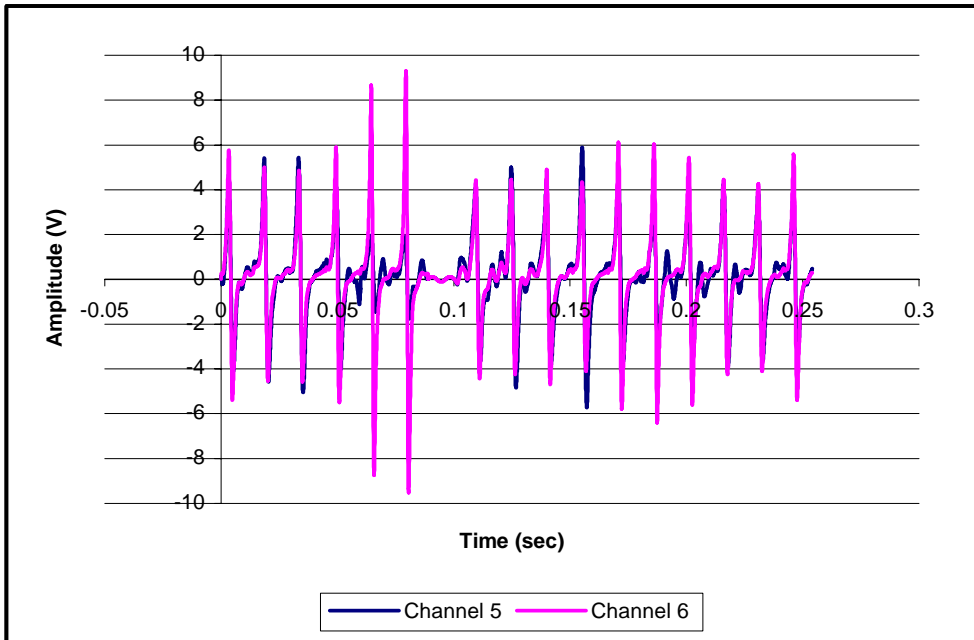
Figure 49. Missing roller probe 5-6
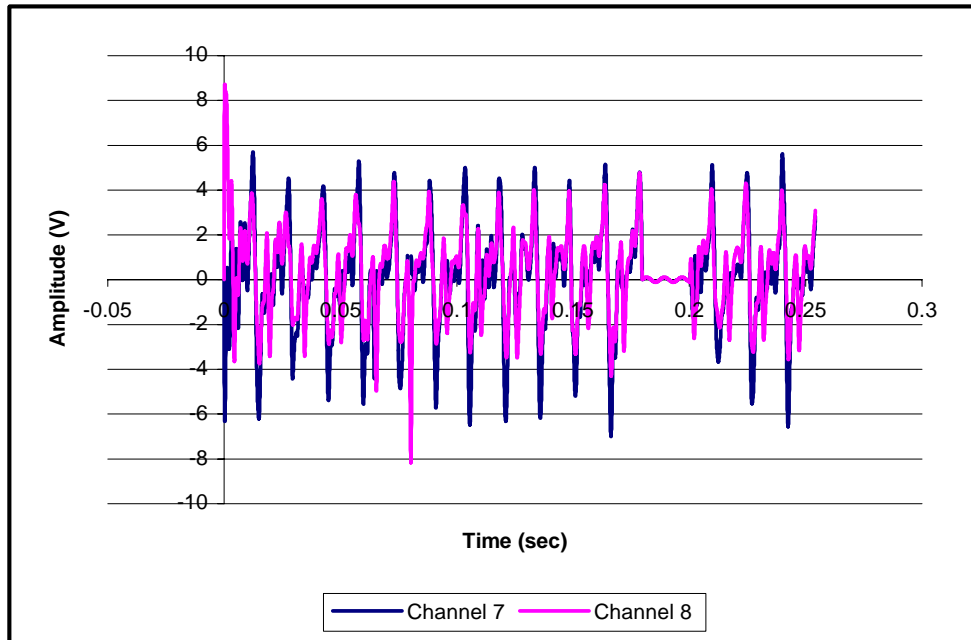
Figure 50. Missing roller channel 7-8

Same Roller Magnitude Test

Tests were performed capturing several bearing rotations in order to compare the signals given by each roller for a period of time. It was found through these experiments that the amplitude of the signal for each individual roller was fairly constant for every probe, signifying that the fly height varied minutely within a roller. Figure 51 to Figure 53 show that this outcome occurred in different loading zone locations and with different radial loads applied. The magnitude variations are noted to be almost non-existent with the application of small radial loads and more frequent with higher applied loads. In the mentioned figures, if the amplitude value for every 16th roller is analyzed and compared to others within the same chart, the relationship already mentioned can be observed.
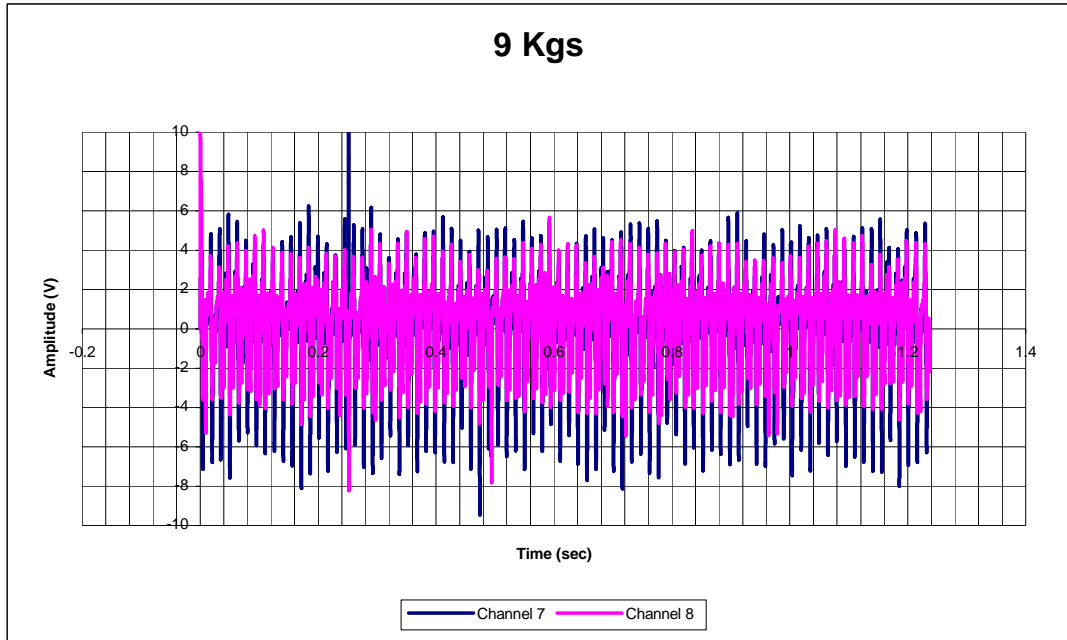
Figure 51. 9Kg Channel 7-8 five cage rotations captured

Figure 52. 273Kg Channel 5-6 five cage rotations captured
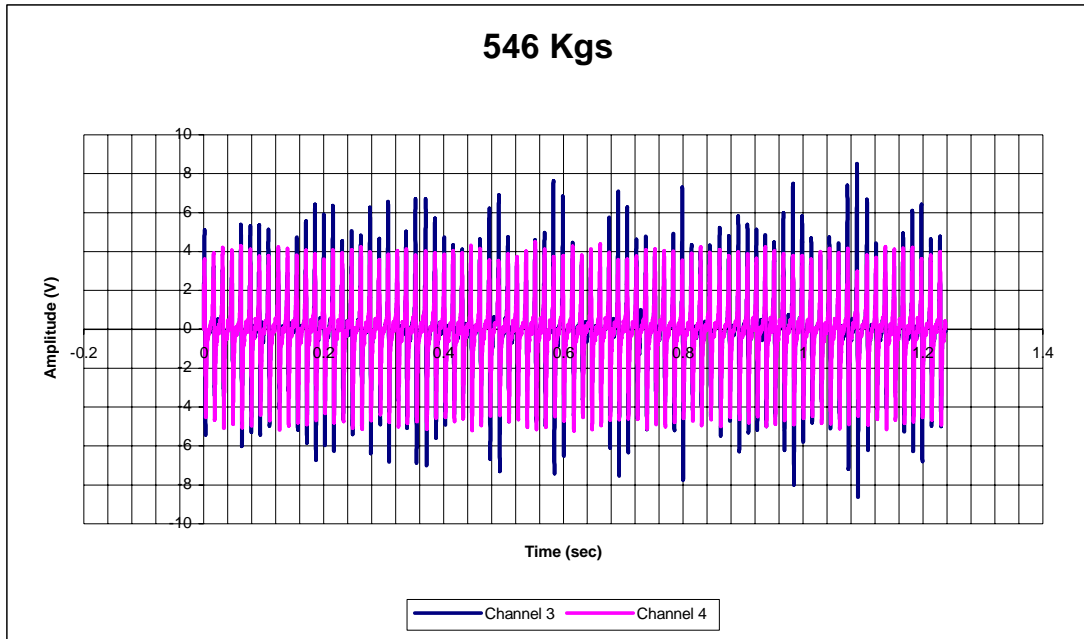
Figure 53. 546Kg Channel 3-4 five cage rotations captured

Individual Roller Measurements

Tests were performed in order to measure the relative skew of each roller at different locations of the loading zone and under different radial loads. The results of some of these tests are displayed in Figure 54 to Figure 56. These figures show that for different loads and at different locations in the load zone the skew measurements of each individual roller can be measured. It needs to be noted that these measurements were taken for five roller rotations per probe, so if only two or three data points are seen per roller, that signifies that five points lie within these values on top of each other. It is also important to note that the spacing between two consecutive measurements is due to the limited resolution of the data acquisition card. If a more capable data acquisition card

70

was used, the distribution of the points in Figure 54 to Figure 56 would be much smaller and tighter.

In order to accurately track each roller as an individual entity, it was necessary to perform a careful waveform analysis in order to maintain the integrity of the observations.
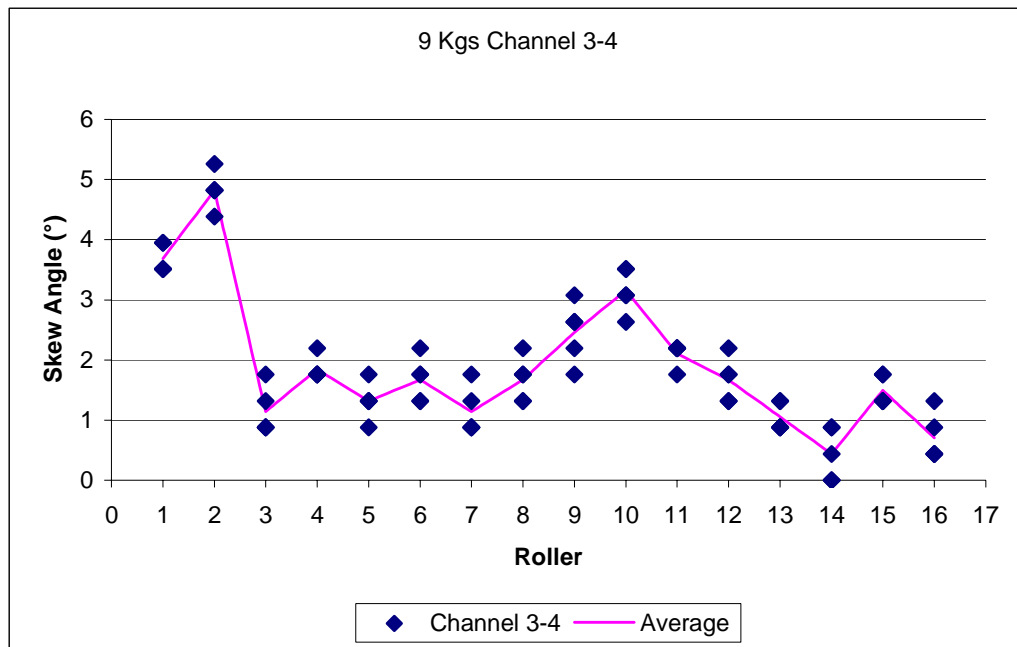
Figure 54. 9Kg Channel 3-4 individual roller skew
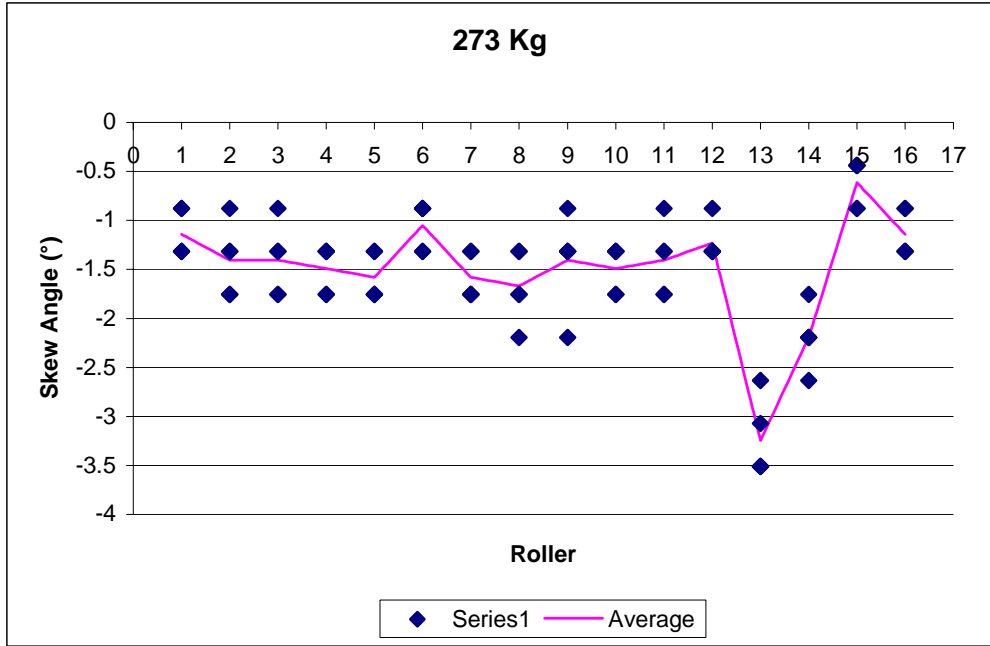
Figure 55. 273Kg Channel 5-6 individual roller skew
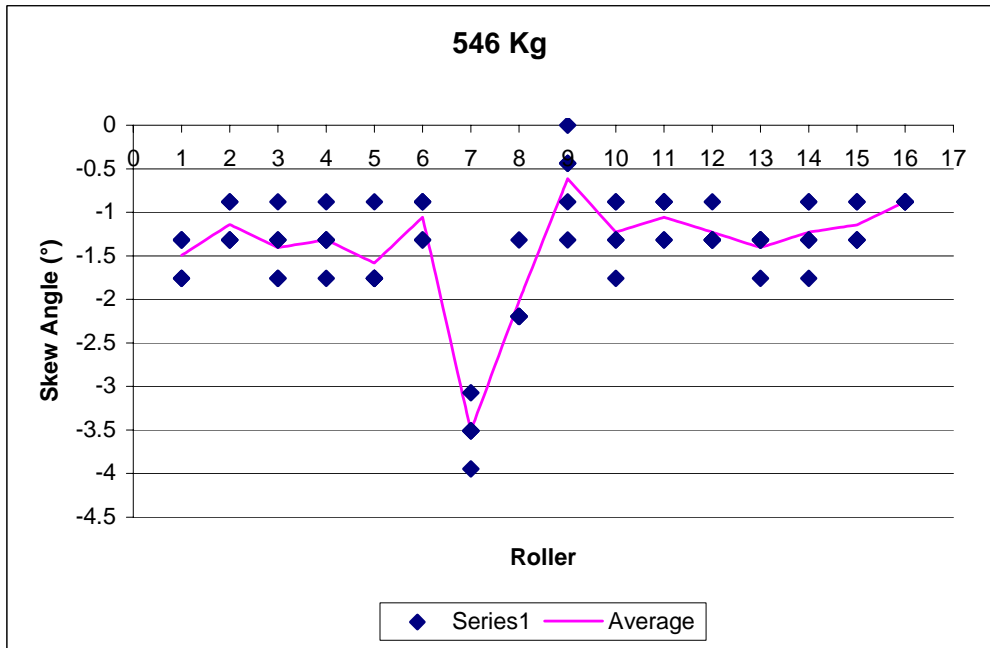
Figure 56. 546Kg Channel 7-8 individual roller skew

72

Overall Bearing Performance

Tests were performed in order to measure the overall skew of the bearing at different locations of the loading zone and subjected to different radial loads. It is noted that the behavior of rollers was the same in terms of roller signature, activity, and skew measurements. The roller signature measurements can be observed in Figure 47 to Figure 56. If a roller was tracked for a limited period of time (this period of time is limited due to the considerable amount of data points that is required per waveform in order to obtain a good resolution) it was observed that the data obtained was consistent for experiments with similar experimental parameters of shaft speed and radial load. From Figure 47 to Figure 50 it was noted that the period of each individual roller waveform was kept constant and therefore the overall bearing revolution period was kept constant. It was also noted from Figure 47 to Figure 50 that the missing roller waveform was always located at the same distance between probe pairs, which denotes that the cage speed was kept constant with constant shaft speed as per Equation 45. Figure 51 to Figure 53 show that the amplitude of the roller signature was kept constant throughout experiments, while consistent values for Figure 54 to Figure 56 portray that the roller skew signature was kept constant with similar shaft speed and radial load values.

The roller activity was also constant within the same loading zone location with similar values of shaft speed and radial load. It was noted that at the maximum loading zone location (probes 3 and 4) the waveforms were clearer and less noisy as seen in Figure 57. A hypothesis of the reason the signal is clearer at the maximum load zone location is because of the stress experienced by the roller when being pressed against the

outer and inner raceways of the bearing. This phenomenon stabilizes the roller and forces it to roll against the surfaces rather than slide and vibrate.
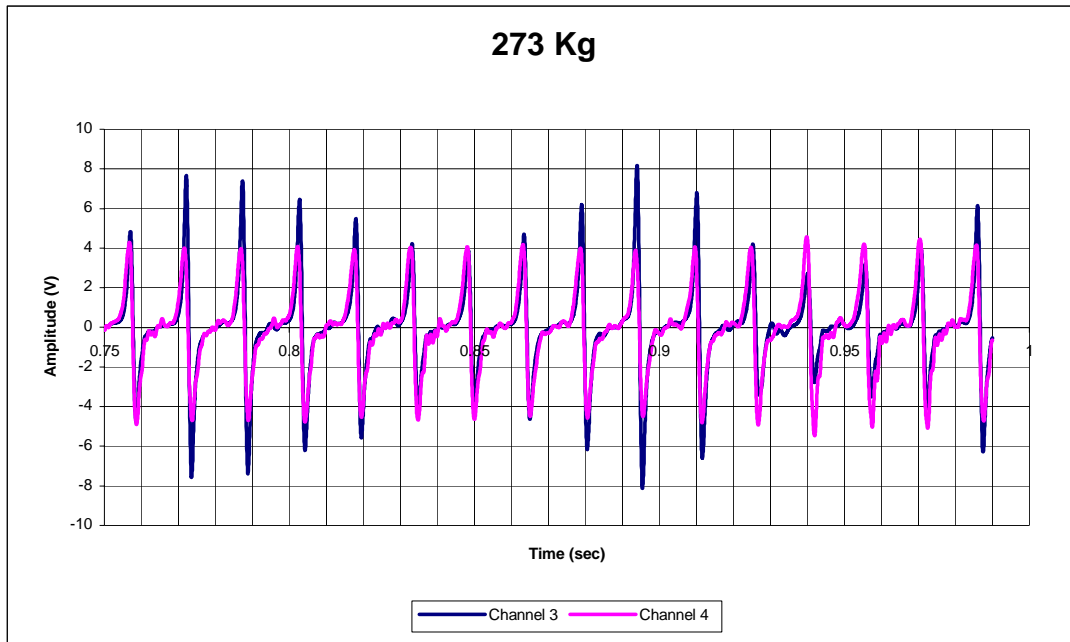
Figure 57. Sample waveform for channels 3-4

Waveforms at the start (probes 1 and 2) and end (probes 5 and 6) of the loading zone were noisier but remained very legible as seen in Figure 58.
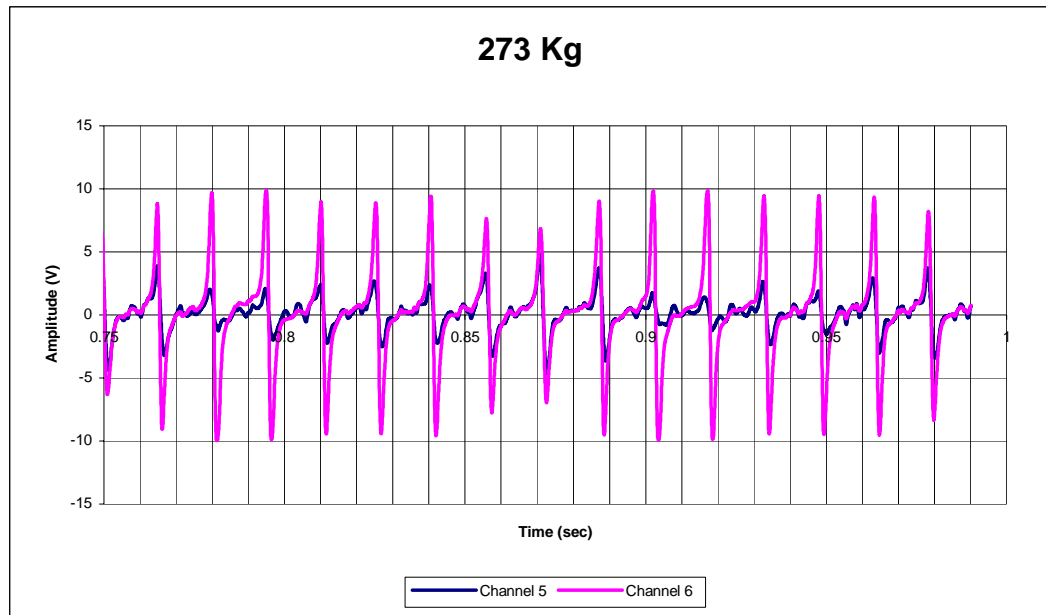
Figure 58. Sample waveform for channels 5-6

Waveforms at the no loading zone (probes 7 and 8) were the noisiest and presented the most problem when performing data processing due to the multiple peaks encountered. These peaks and noise are the result of roller vibrations most likely due to the lack of compressing forces between the outer raceway (where the probes are located) and the rollers. A sample waveform is displayed in Figure 59.
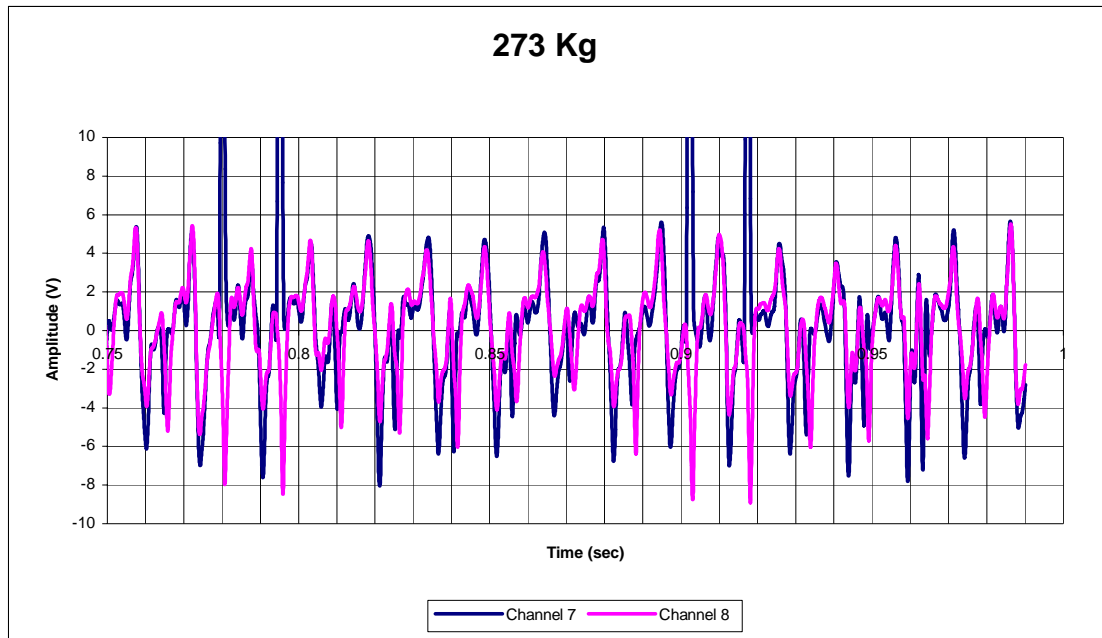
Figure 59. Sample waveform for channels 7-8

After several repetitions, it was observed that the overall skew measurements at different locations of the loading zone were consistent between measurements. Figure 60 displays a typical bearing skew measurement for the bearing overall. The overall bearing skew is measured by averaging the skew of the rollers after several cage rotations. In the case of Figure 60, five cage rotations (or 80 consecutive rollers) were averaged. It can be noted that Channel 3-4 had the least skew difference between 0Kg and 546Kg and Channel 7-8 had the most. Averaging the skew of all rollers for several bearing rotations is a legitimate way to represent the data for the entire bearing since it has been shown previously that characterization of individual rollers can yield a difference in roller skew depending on each individual roller. By taking the average of several complete bearing rotations a characterization of the bearing as a whole can be made.
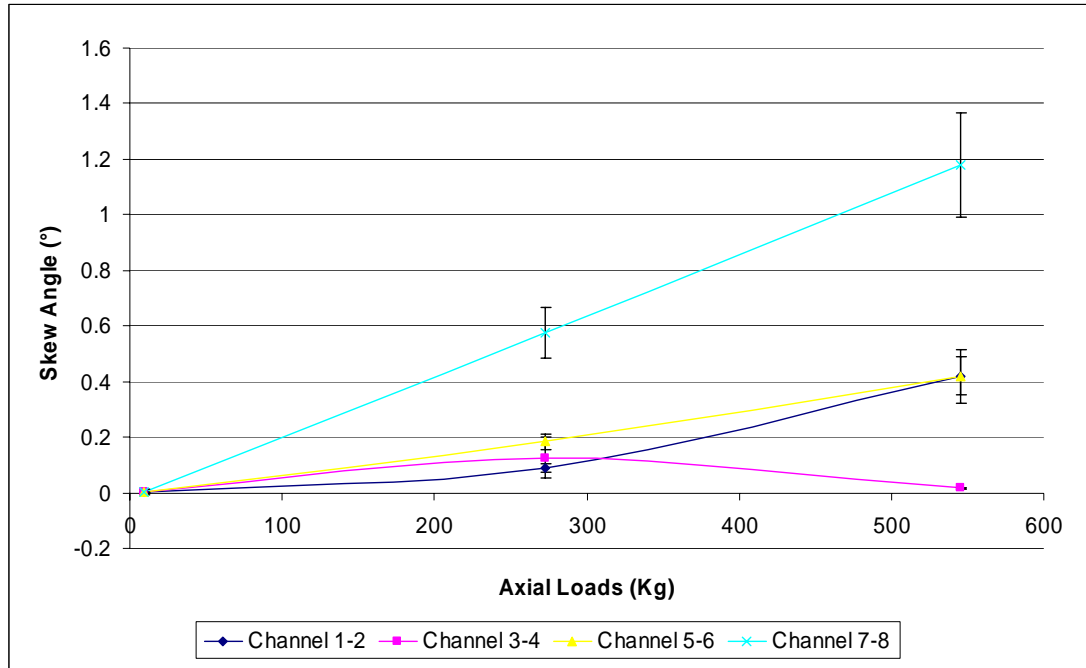
Figure 60. Bearing overall skew measurements

Forward-Backward Test

Tests were performed with the motor running forward (clockwise rotation of the bearing) and backward (counter-clockwise rotation of the bearing) in order to validate that the time/phase measurements are independent of the sensor location. It was important to run the forward-backward test to identify probe misalignment which can lead to erroneous interpretations of roller skew. By running these set of tests, probe misalignment can be cancelled out and corrected if desired. Running these tests would also provide a stronger ground to corroborate the veracity of the data previously obtained.

It was found that the individual roller skew was maintained constant for identical experimental conditions with the only exception that the graphs between clockwise and counterclockwise rotation were mirrored and in reverse order (as expected because of the reverse order at which the roller passes the probe pair). Figure 61 to Figure 66 display

the results for different radial loads applied in a clockwise rotation compared to the results obtained for counter-clockwise rotation. The x-axis for the charts with counter-clockwise shaft rotation was changed to match the rollers with the legend of the clockwise shaft rotation x-axis. It can be observed in Figure 61 to Figure 66 that each individual roller's skew is measured for five bearing rotations and separately plotted for each roller (if fewer than 5 points are observed per roller it's because some data points lie on top of others). An average line was plotted across the graph identifying the average measurement for each roller's skew measurements. By comparing the overall silhouette of the data between the clockwise and counter-clockwise it can be observed that a strong correlation exists between both graphs, and a probe misalignment can be observed as the average offset between both graphs with respect to the x-axis.

The phenomena described in this section can be observed at all instances of the loading zone and at varying speeds and loads. It should be noted that at higher rotational speeds the resolution of the system is decreased due to a faster rotation with constant acquisition frequency established by the limitations of the data acquisition card.
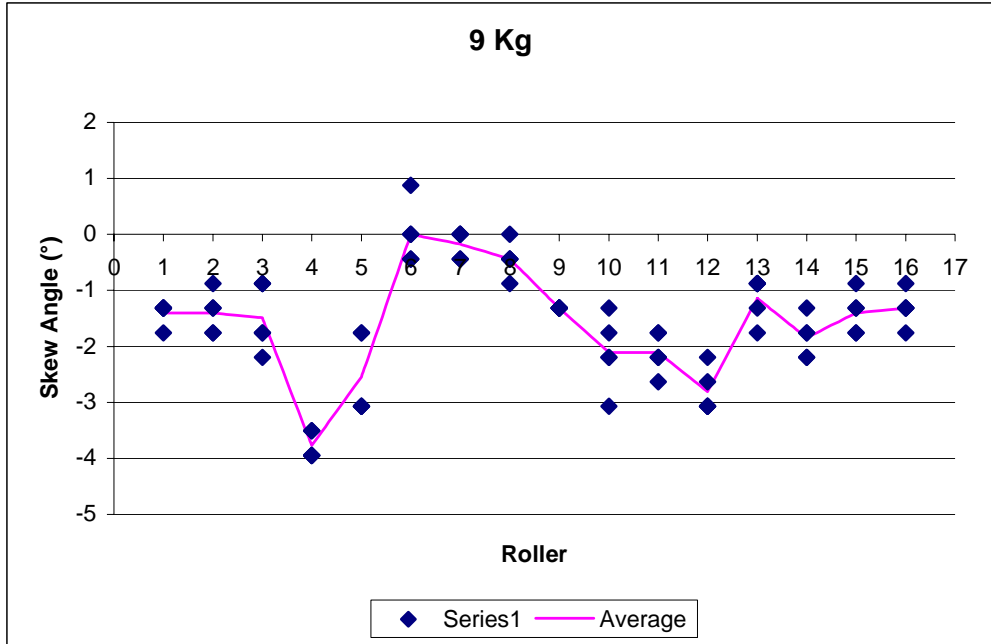
**Figure 61. Forward (clockwise) 9Kg individual roller skew**
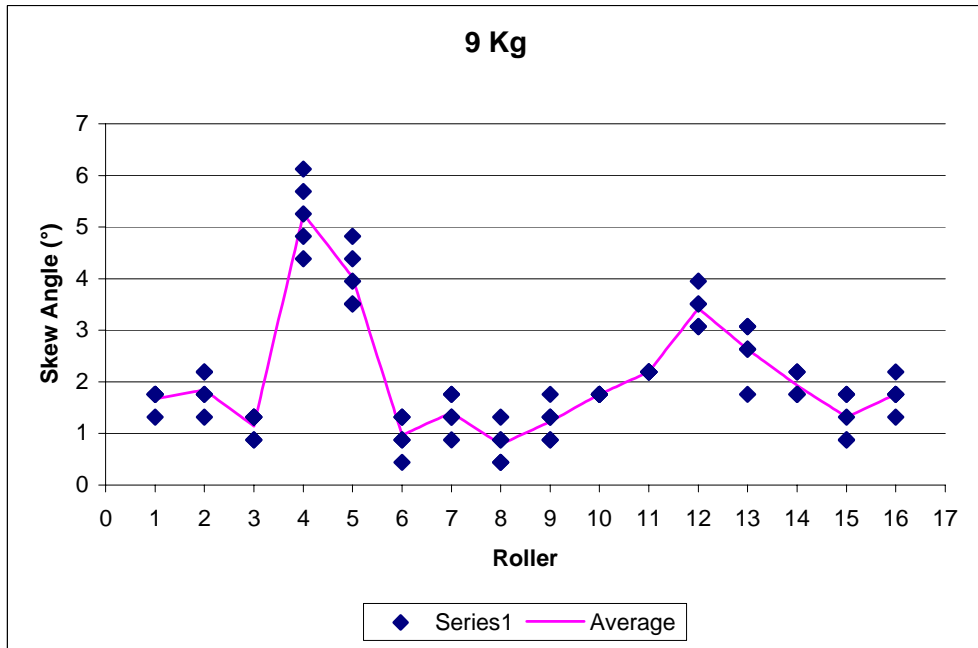
Figure 62. Backward (counter-clockwise) 9Kg individual roller skew
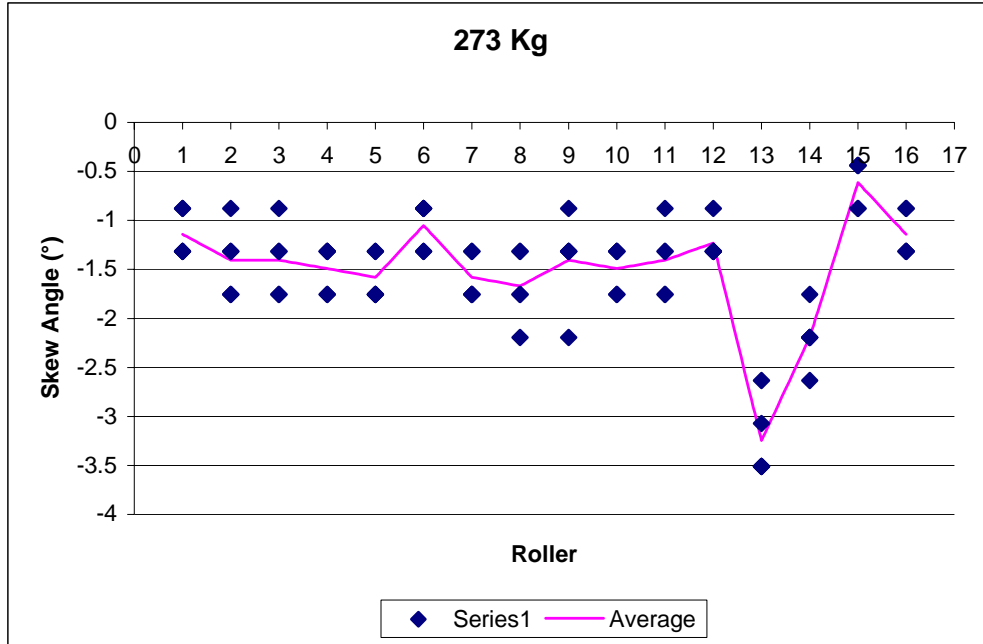
Figure 63. Forward (clockwise) 273Kg individual roller skew
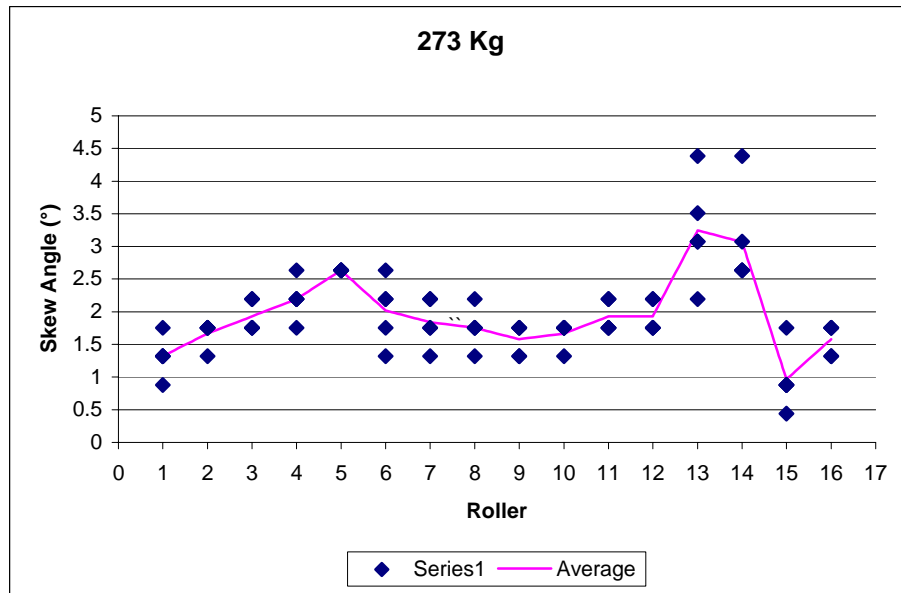
Figure 64. Backward (counter-clockwise) 273Kg individual roller skew
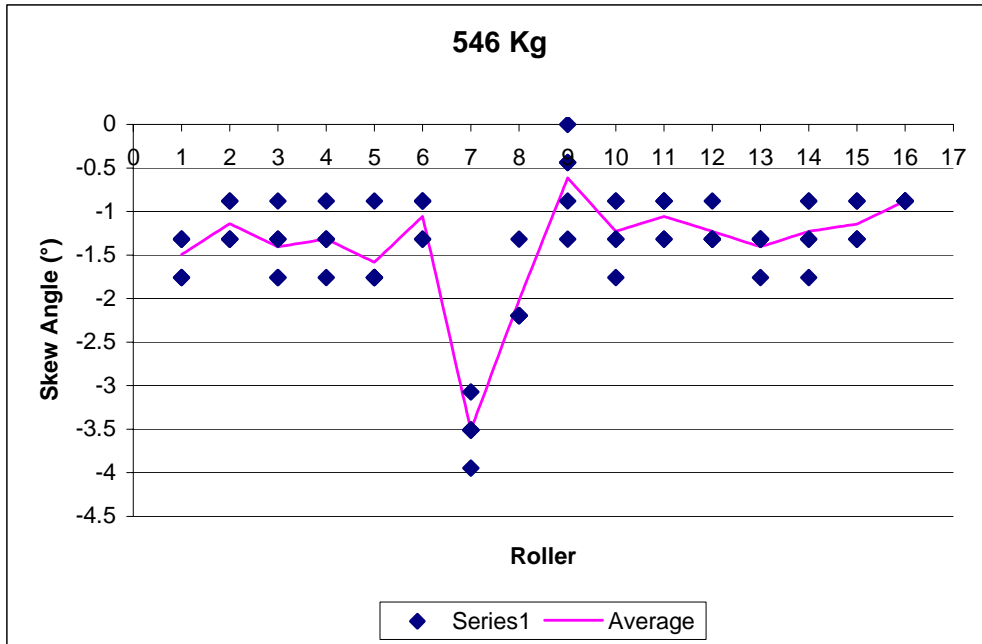
Figure 65. Forward (clockwise) 546Kg individual roller skew
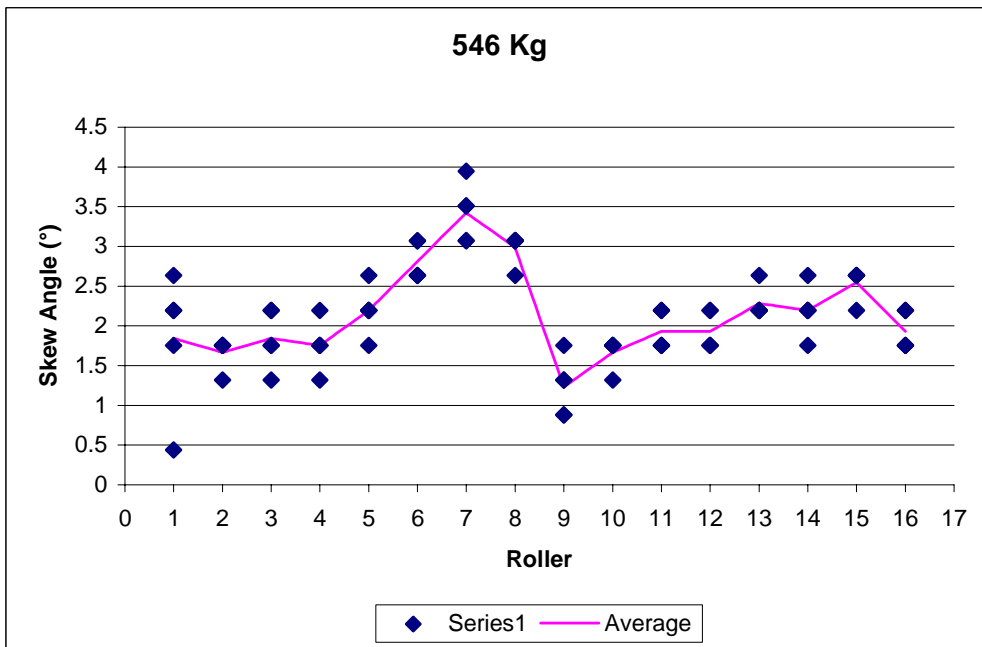
Figure 66. Backward (counter-clockwise) 546Kg individual roller skew

CHAPTER 6

DISCUSSION OF RESULTS

This chapter will discuss the results previously shown. It will illustrate the importance of each test and the outcome of the preliminary observations. This chapter is then followed by a chapter with conclusions drawn from all the data gathered.

CPD Waveform Shape

The obtained waveform shape from the Contact Potential Difference probes correlates with the predicted shape shown in Figure 6. By comparing the shape of the CPD signal obtained by the predicting model to the sample signals found in Figure 57 to Figure 59, it is observed that the their profile is very similar.

CPD Dependence on Frequency

Based on the results obtained from the frequency response tests and on the calculations previously done, theoretical limits for the shaft speed were calculated. In order to perform experiments within the flat range of the gain curves displayed in Figure 45, the revolutions of the shaft need to be between 600 RPM and 10,000 RPM.

The importance of characterizing the influence on the probes' signal generated by the experimental frequency is observed in the results obtained. For the case of many CPD experiments, the amplitude gain of the signal is important to obtain accurate results.

It is therefore equally important to design the probe for the experiment as it is to design the experiment for the probe.

Missing Roller Experiment

Based on the results obtained from the missing roller experiments, it is an obvious observation that a roller missing in the bearing can be detected. Although this conclusion is evident, the consequences and ramifications of this experiment are far more enriching. This experiment shows that a single roller defect can be observed by monitoring the bearing motion using a CPD probe. Roller defects can be categorized from an ample range of geometric flaws to imperfections such as scratches, indentations, or wear created by the bearing motion. From the results it was also noted that the waveform of the missing roller was always located at the same distance between probe pairs, which denotes that the cage speed was kept constant with constant shaft speed.

Same Roller Magnitude Test

Based on the results obtained from the same roller magnitude experiments, it was observed that throughout the revolutions of the shaft, the magnitude of the CPD signal obtained from a roller was kept constant. This proves that the fly height of the roller did not change when maintaining the same radial load at a constant shaft speed. This result shows that the roller's fly height is kept constant by the compressive stresses of the raceways in the bearing.

Individual Roller Measurements

Based on the results obtained from the individual roller measurements, it can be inferred that for different loads and at different locations of the load zone the skew measurements per roller are consistent when maintaining the same radial load at a constant shaft speed. These results show that the spacing between the measurements taken by the probes is within a resolution mark of the next. Due to this finding, it is obvious to observe that with a higher resolution data acquisition card, the distribution of the points would be tighter. The results for this experiment along with those of "Same Roller Magnitude Test" also set a precedent in roller bearing analysis where individual roller "signature" can be obtained and examined in order to obtain a more in depth understanding of bearing behavior along with a general bearing health.

Overall bearing performance

Based on the results obtained from the overall bearing performance tests, it can be seen that the predicted CPD signal shape for this probe is obtained in every roller. It can also be observed from the results that individual roller "signature" is maintained throughout the experiments and that the period of each individual roller waveform was kept constant and therefore the overall bearing revolution period was kept constant.

From the results it was also observed that the roller activity was constant within the same loading zone location with similar values of shaft speed and radial load. It was noted that at the maximum loading zone location (probes 3 and 4) the waveforms were clearer and less noisy and the noisiest at the no loading zone (probes 7 and 8).

Most importantly, from the results of these tests and Figure 60, it was observed that the overall skew of the bearing had its maximum deviation between the 0Kg and 546Kg loads at the no load zone with a skew angle measurement of 1.10°, followed by a skew of .039° and 0.40° at the beginning and end of the load zone respectively, and a minimum skew angle measurement of 0.016° at the maximum load zone location.

These values and skew distribution profile around the bearing obtained from these experiments compare to those found by NSK in 2000 [23]. The skew profiles shown by the experimental results, and those found by NSK are similar in magnitude and in verifying that at the maximum loading zone there is little to no roller skew present. At the beginning and end of the loading zone there is some roller skew present, and at the no loading zone there is significant skew.

Forward-Backward Test

The results obtained from the forward-backward tests strengthen the point that a roller "signature" is present at the same point of the loading zone with constant load and shaft speed. The results also show that running the experiments forward and backward does not change the outcome of the skew measurements, only the direction in which skew is measured. Running the experiments forward and backward is very useful to measure skew because if the probes are misaligned with respect to each other, this misalignment would show as part of the skew results in one direction, but can be corrected when equilibrating with the results obtained from measuring in the other direction.

The results displayed under this section are the main contribution of this thesis to the bearing monitoring and analysis field. Utilizing the CPD technique portrayed in this thesis, it has been proven that not only can roller skew be calculated, but also individual roller monitoring can be accomplished. Individual roller monitoring can be used to improve the construction of bearings and for quality control purposes. Since this discovery is novel to the bearing field, there is no data comparison that can be done and the repeatability of the experiments suffices as a validation of the phenomenon. Further experiments are required in order to expand this area into a new and very promising part of bearing analysis.

CHAPTER 7

CONCLUSIONS

This research shows that a pair of specialized Contact Potential Difference probes and circuitry can be customized to obtain overall bearing measurements as well as individual roller information for the in-situ monitoring of bearings and rollers. The following conclusions were drawn from this thesis:

1. The bearing roller skew increases as the shaft speed increases.

2. The bearing roller skew increases as the applied radial load increases.

3. The bearing roller skew is greatest at the no load zone location with a skew angle measurement of 1.10° and smallest at the maximum load zone location with a skew angle measurement of 0.016°. It is also noted that at the beginning and end of the load zone the magnitude of the skew measurements is almost the same with skew measurements of .0.39° and 0.40° respectively.

4. Different rollers' skew is different within a bearing under equal experimental conditions, but the behavior of individual rollers does not change significantly within themselves. This phenomenon allows for the creating of a "roller signature" which is used to identify the signal characteristics of each roller.

RECOMMENDATIONS

Recommendations are made in this chapter in order to further improve the system and apply this thesis' findings into new areas:

1. Investigate the feasibility of utilizing a more capable data acquisition card which can deliver a higher resolution for the experiments. This new data acquisition would provide more accurate data that will have smaller distributions.

2. The implementation of a different data processing technique, especially if a higher resolution data acquisition card is used. The amounts of data points required for efficiently measuring several CPD probes with a high resolution is extensive. Ideally the new data processing technique would include custom filters to reduce high frequency noise along with routine calculations to automatically calculate roller skew, with little human interaction.

3. The implementation of software that reads information from the DAQ card for each roller and immediately graphs the current state of the roller, and any pertinent information calculated from the measurement. As the same roller passes by the probe, the program updates the information and performs roller history analysis.

4. Develop film thickness CPD probes that can be mounted inside the outer raceway of a bearing in order to in-situ measure skew and roller behavior without machining the bearing. Another option is to build CPD probes just like the ones shown in this thesis into the surface of the bearing outer raceway and with the use of gaskets and machining, replace 100% of the material removed with CPD

sensor material in order to not alter the geometry of the bearing while utilizing strong materials that will provide the required bearing strength.

APPENDIX A

## CPD Bearing Software User Interface
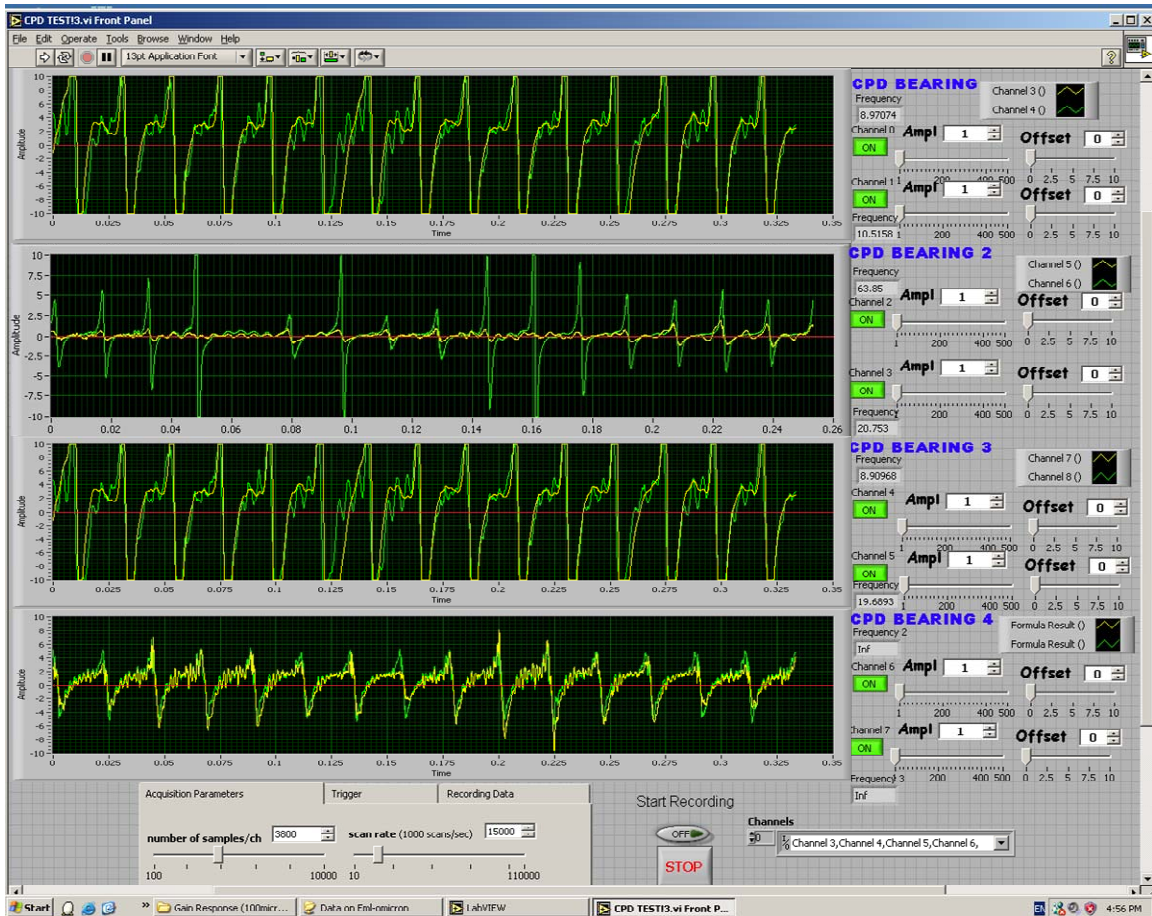

Figure 67. LabVIEW CPD Bearing User Interface

Figure 68. CPD Bearing Software Wire Diagram

# Load Cell Calibration Curve
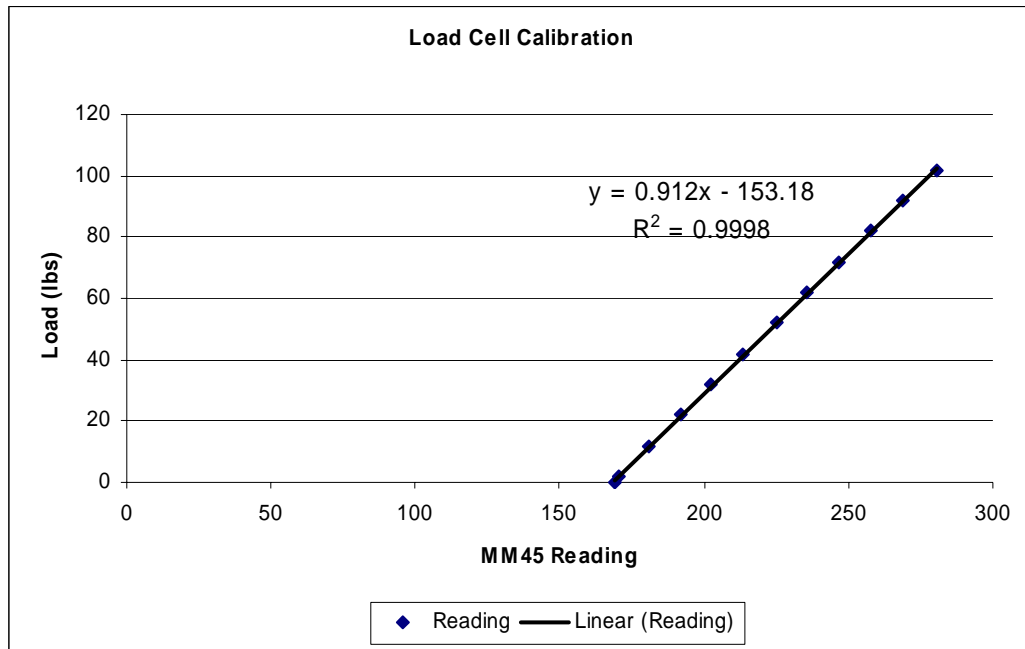
Figure 69. Load cell calibration data

Matlab Filtering Program for 2 Probes

```matlab
clear all
close all

[filename, filepath]=uigetfile('*.txt','Select File')

%[A,B] = XLSREAD('','SHEETNAME')
[time,channel1,channel2] = textread(filename,'%n%n%n%*[^\n]','delimiter',',');

windowsize=5;

filter0=filter(ones(1,windowsize)/windowsize,1,time);
filter1=filter(ones(1,windowsize)/windowsize,1,channel1);
filter2=filter(ones(1,windowsize)/windowsize,1,channel2);

for j=1:10
filter0=filter(ones(1,windowsize)/windowsize,1,filter0);
filter1=filter(ones(1,windowsize)/windowsize,1,filter1);
filter2=filter(ones(1,windowsize)/windowsize,1,filter2);
end

% cftool

figure;plot(filter0,filter1);
hold on;
plot(filter0,filter2,'r');
hold off;

A=[filter0,filter1,filter2];
s='.xls';
s = strcat(filename,s);

%[SUCCESS,MESSAGE]=xlswrite(s,A,filename);
[SUCCESS,MESSAGE]=xlswrite('Filtered.xls',A,filename);

%fid = fopen(s, 'w');
%fprintf(fid,'%6.8f  %6.8f\n',A);
%fclose(fid);
```

Matlab Filtering Program for 6 Probes

```matlab
clear all
close all

[filename, filepath]=uigetfile('*.txt','Select File')

[time,channel1,channel2,channel3,channel4,channel5,channel6] =
textread(filename,'%n%n%n%n%n%n%n%*[^\n]','delimiter',',');

windowsize=5;

filter0=filter(ones(1,windowsize)/windowsize,1,time);
filter1=filter(ones(1,windowsize)/windowsize,1,channel1);
filter2=filter(ones(1,windowsize)/windowsize,1,channel2);
filter3=filter(ones(1,windowsize)/windowsize,1,channel3);
filter4=filter(ones(1,windowsize)/windowsize,1,channel4);
filter5=filter(ones(1,windowsize)/windowsize,1,channel5);
filter6=filter(ones(1,windowsize)/windowsize,1,channel6);

for j=1:10
filter0=filter(ones(1,windowsize)/windowsize,1,filter0);
filter1=filter(ones(1,windowsize)/windowsize,1,filter1);
filter2=filter(ones(1,windowsize)/windowsize,1,filter2);
filter3=filter(ones(1,windowsize)/windowsize,1,filter3);
filter4=filter(ones(1,windowsize)/windowsize,1,filter4);
filter5=filter(ones(1,windowsize)/windowsize,1,filter5);
filter6=filter(ones(1,windowsize)/windowsize,1,filter6);
end

plot(filter0,filter1);print;
hold on;
plot(filter0,filter2,'r');print;
hold off;

plot(filter0,filter3);print;
hold on;
print;plot(filter0,filter4,'r');
hold off;

plot(filter0,filter5);print;
hold on;
plot(filter0,filter6,'r');print;
hold off;

A=[filter0,filter1,filter2,filter3,filter4,filter5,filter6];
s='.xls';
s = strcat(filename,s);

[SUCCESS,MESSAGE]=xlswrite('Filtered.xls',A,filename);
```

Matlab Filtering Program for 8 Probes

```matlab
clear all
close all

[filename, filepath]=uigetfile('*.txt','Select File')

[time,channel1,channel2,channel3,channel4,channel5,channel6,channel7,channel8] =
textread(filename,'%n%n%n%n%n%n%n%n%n%*[^\n]','delimiter',',');

windowsize=5;

filter0=filter(ones(1,windowsize)/windowsize,1,time);
filter1=filter(ones(1,windowsize)/windowsize,1,channel1);
filter2=filter(ones(1,windowsize)/windowsize,1,channel2);
filter3=filter(ones(1,windowsize)/windowsize,1,channel3);
filter4=filter(ones(1,windowsize)/windowsize,1,channel4);
filter5=filter(ones(1,windowsize)/windowsize,1,channel5);
filter6=filter(ones(1,windowsize)/windowsize,1,channel6);
filter7=filter(ones(1,windowsize)/windowsize,1,channel7);
filter8=filter(ones(1,windowsize)/windowsize,1,channel8);


for j=1:10
filter0=filter(ones(1,windowsize)/windowsize,1,filter0);
filter1=filter(ones(1,windowsize)/windowsize,1,filter1);
filter2=filter(ones(1,windowsize)/windowsize,1,filter2);
filter3=filter(ones(1,windowsize)/windowsize,1,filter3);
filter4=filter(ones(1,windowsize)/windowsize,1,filter4);
filter5=filter(ones(1,windowsize)/windowsize,1,filter5);
filter6=filter(ones(1,windowsize)/windowsize,1,filter6);
filter7=filter(ones(1,windowsize)/windowsize,1,filter7);
filter8=filter(ones(1,windowsize)/windowsize,1,filter8);
end

A=[filter0,filter1,filter2,filter3,filter4,filter5,filter6,filter7,filter8];
s='.xls';
s = strcat(filename,s);

[SUCCESS,MESSAGE]=xlswrite('Filtered.xls',A,filename);
```

REFERENCES

[1] N. Ashcroft and N. Mermin, *Solid State Physics*. Holt: New York, 1976.

[2] L. Kelvin, G. Fitzgerald, and W. Francis, "Contact Electricity of Metals." Philosophical Magazine and Journal of Science, (1898): 80-120.

[3] W. A. Zisman, "A New Method of Measuring Contact Potential difference in Metals." Scientific Instruments, 3, (1967): 367-370.

[4] E. Zanoria, K. Hamall, S. Danyluk, and A.L. Zharin, "The Non-vibrating Kelvin Probe and its Application for Monitoring Surface Wear." Journal of Testing and Evaluation, 25, (1997): 233-238.

[5] Y. Yang, S. Danyluk, and M. Hoeprich, "A Study on Rolling Element Skew Measurement in a Tapered Roller Bearing With a Specialized Capacitance Probe." Transactions of the ASME, 122, (2000): 534-538.

[6] Hoeprich, Mike. "Probe Signal". Personal email. 2006.

[7] The Torrington Company – Service Catalog.

[8] Harris, T.A., *Rolling Bearing Analysis,* John Wiley, 1991.

[9] Eschmann, Hasbargen, and Weigand., *Ball and Roller Bearings Theory, Design, and Application,* John Wiley, 1985.

[10] Roelands, C.J.A., "Correlational Aspects of Viscosity-Temperature-Pressure Relationship of Lubricating oils", *Druk,* V.R.B. (1966)

[11] S.Bair, and F. Qureshi, "The Generalized Newtonian Fluid Model and Elastohydrodynamic Film Thickness." Transactions of the ASME, 125, (2003): 70-75.

[12] Dowson, D., and Toyoda, S., 1979 "A Central Film Thickness Formula for Elastohydrodynamic Contacts," *Elastohydrodynamics and Related Topics*, Dowson, Taylor, Godet and Berthe, eds., pp.60-65

[13] Dowson, D., and Higgison, G.R., 1966, *Elastohydrodynamic Lubrication*, Pergamon Press, Oxford

[14] Hamrock, B., *Fundamentals of Fluid Lubrication,* McGraw-Hill, 1994.

[15] D. Yano, C. Korach, J.Streator, and S. Danyluk, "Nonvibrating Contact Potential Difference Probe Measurement of a Nanometer-Scale Lubricant on a Hard Disk." Transactions of the ASME, 121, (1999): 980-983.

[16] L. Ellis, "Oil monitoring with an optically stimulated contact potential difference sensor," Masters Thesis, Georgia Institute of Technology, 2004.

[17] National Instruments Corporation – PCI E Series User Manual, 1997.

[18] A. Watt, "Fringer field corrections in nvCPD applications," Masters Thesis, Georgia Institute of Technology, 2004.

[19] ENTRAN Devices – Instruction Manual for MM45 Rev. A Series Sensor Monitor/Excitation, 1996.

[20] Singmin, Andrew., *Modern Electronics Soldering Techniques,* Prompt (DPI - 8/01), 2000.

[21] Kotzalas, Mike. "SRB Project Gatech." Personal email. 2004-2006.

[22] Bevington, Philip R., *Data reduction and error analysis for the physical sciences,* McGraw-Hill, 1992.

[23] A.Honda, A. Miyasaka, and M. Matsubara, "EA Spherical Roller Bearings." Motion & Control, No.9, (2000): 1-6.